



LJMU Research Online

McLeod, AF, Kruijssen, JMD, Weisz, DR, Zeidler, P, Schruha, A, Dalcanton, JJ, Longmore, SN, Chevance, M, Faesi, CM and Byler, N

Stellar Feedback and Resolved Stellar IFU Spectroscopy in the nearby Spiral Galaxy NGC 300

<http://researchonline.ljmu.ac.uk/id/eprint/11660/>

Article

Citation (please note it is advisable to refer to the publisher's version if you intend to cite from this work)

McLeod, AF, Kruijssen, JMD, Weisz, DR, Zeidler, P, Schruha, A, Dalcanton, JJ, Longmore, SN, Chevance, M, Faesi, CM and Byler, N (2020) Stellar Feedback and Resolved Stellar IFU Spectroscopy in the nearby Spiral Galaxy NGC 300. The Astrophysical Journal. 891 (1). ISSN 1538-4357

LJMU has developed **LJMU Research Online** for users to access the research output of the University more effectively. Copyright © and Moral Rights for the papers on this site are retained by the individual authors and/or other copyright owners. Users may download and/or print one copy of any article(s) in LJMU Research Online to facilitate their private study or for non-commercial research. You may not engage in further distribution of the material or use it for any profit-making activities or any commercial gain.








The version presented here may differ from the published version or from the version of the record. Please see the repository URL above for details on accessing the published version and note that access may require a subscription.

For more information please contact researchonline@ljmu.ac.uk

<http://researchonline.ljmu.ac.uk/>



Stellar Feedback and Resolved Stellar IFU Spectroscopy in the Nearby Spiral Galaxy NGC 300

Anna F. McLeod^{1,2} , J. M. Diederik Kruijssen³, Daniel R. Weisz¹ , Peter Zeidler^{4,5} , Andreas Schrubba⁶, Julianne J. Dalcanton⁷ , Steven N. Longmore⁸ , Mélanie Chevance³, Christopher M. Faesi^{9,10} , and Nell Byler^{11,12} 

¹ Department of Astronomy, University of California Berkeley, Berkeley, CA 94720, USA; anna.mcleod@berkeley.edu, anna.mcleod@ttu.edu

² Department of Physics & Astronomy, Texas Tech University, P.O. Box 41051, Lubbock, TX 79409, USA

³ Astronomisches Rechen-Institut, Zentrum für Astronomie der Universität Heidelberg, Mönchhofstraße 12-14, D-69120 Heidelberg, Germany

⁴ Department of Physics and Astronomy, Johns Hopkins University, Baltimore, MD 21218, USA

⁵ Space Telescope Science Institute, 3700 San Martin Drive, Baltimore, MD 21218, USA

⁶ Max-Planck-Institut für extraterrestrische Physik, Giessenbachstraße 1, D-85748 Garching, Germany

⁷ Department of Astronomy, University of Washington, Box 351580, Seattle, WA 98195, USA

⁸ Astrophysics Research Institute, Liverpool John Moores University, Liverpool, L3 5RF, UK

⁹ Max Planck Institute for Astronomy, Königstuhl 17, D-69117 Heidelberg, Germany

¹⁰ Department of Astronomy, University of Massachusetts—Amherst, Amherst, MA 01003, USA

¹¹ Research School of Astronomy and Astrophysics, The Australian National University, ACT, Australia

¹² ARC Centre of Excellence for All Sky Astrophysics in 3 Dimensions (ASTRO 3D), Australia

Received 2019 October 16; revised 2020 January 16; accepted 2020 January 16; published 2020 February 28

Abstract

We present MUSE integral field unit (IFU) observations of five individual H II regions in two giant star-forming complexes in the low-metallicity, nearby dwarf spiral galaxy NGC 300. In combination with high spatial resolution *Hubble Space Telescope* photometry, we demonstrate the extraction of stellar spectra and classification of individual stars from ground-based IFU data at the distance of 2 Mpc. For the two star-forming complexes, in which no O-type stars had previously been identified, we find a total of 13 newly identified O-type stars and 4 Wolf-Rayet stars (two already-known sources and two Wolf-Rayet star candidates that this work has now confirmed). We use the derived massive stellar content to analyze the impact of stellar feedback on the H II regions. As already found for H II regions in the Magellanic Clouds, the dynamics of the analyzed NGC 300 H II regions are dominated by a combination of the pressure of the ionized gas and stellar winds. Moreover, we analyze the relation between the star formation rate and the pressure of the ionized gas as derived from small (<100 pc) scales, both quantities being systematically overestimated when derived on galactic scales. With the wealth of upcoming IFU instruments and programs, this study serves as a pathfinder for the systematic investigation of resolved stellar feedback in nearby galaxies, delivering the necessary analysis tools to enable massive stellar content and feedback studies sampling an unprecedented range of H II region properties across entire galaxies in the nearby universe.

Unified Astronomy Thesaurus concepts: Intergalactic medium (813); Galactic and extragalactic astronomy (563); Stellar feedback (1602); Massive stars (732); Young massive clusters (2049); H II regions (694)

1. Introduction

Feedback from massive ($>8 M_{\odot}$) stars is the main driver of secular evolution in galaxies with masses similar to or smaller than the Milky Way (MW). Indeed, state-of-the-art numerical simulations of star-forming molecular clouds (e.g., Bate 2009; Dale et al. 2014) and galaxy evolution (e.g., Vogelsberger et al. 2014; Schaye et al. 2015) cannot reproduce key observables (e.g., the star formation rate [SFR] vs. stellar mass relation; Noeske et al. 2007) without accounting for stellar feedback. Therefore, feedback from massive stars represents one of the main uncertainties in numerical star formation and galaxy evolution studies.

Stellar feedback (e.g., protostellar jets, ionizing radiation, stellar winds, supernovae; see Krumholz et al. 2014) is known to operate on individual cloud scales (roughly tens of parsecs), and numerical simulations have shown that they can shape galaxy properties on global (\sim kiloparsec) scales (e.g., Scannapieco et al. 2012; Hopkins et al. 2013). While there is a good *qualitative* understanding of the physical mechanisms that connect these two scales, the field is lacking *quantitative* observations that directly link the effect of feedback to individual massive stars (or massive stellar populations).

The dynamics of H II regions are governed by a combination of ionizing radiation, winds, and supernovae (McKee et al. 1984), but disentangling the various feedback mechanisms, which often act simultaneously and possibly on relatively short timescales (e.g., supernovae), is observationally challenging (e.g., Lopez et al. 2014). Moreover, while feedback studies of a few individual, nearby (MW and Magellanic Clouds) H II regions exist (e.g., Smith & Brooks 2008; Pellegrini et al. 2010; McLeod et al. 2015, 2016, 2019), due to observational limitations such as small fields of view and large distance uncertainties, most lack the simultaneous *detailed* knowledge of the gas (i.e., properties and kinematics) and the feedback-driving massive stars (i.e., number and spectral type) on which physical H II region properties (e.g., luminosity, temperature, expansion rate) critically depend. This observational characterization of both the sources and the effects of stellar feedback is absolutely critical to measure the fraction of feedback energy and momentum that couples to the surrounding medium (sometimes referred to as the “feedback efficiency”; e.g., Crain et al. 2015; Kruijssen et al. 2018). Observationally, this quantity can be traced by comparing the ionizing photon output of a young stellar population to the observed H α luminosity of the surrounding H II region.

In a recent study, McLeod et al. (2019, hereafter MC19) showcased the capability of integral field units (IFUs) to spectroscopically identify and classify massive stars within H II regions, while simultaneously deriving feedback-related quantities. Using the optical IFU Multi Unit Spectroscopic Explorer (MUSE) on the Very Large Telescope, MC19 studied a total of 11 individual H II regions in the Large Magellanic Cloud (LMC) in terms of their massive stellar content and the related effect of stellar feedback, finding that (i) the expansion of the H II regions is driven by winds and the pressure of the ionized gas and (ii) feedback has a negative effect on star formation (i.e., quenching).

Quantifying the influence of feedback from massive stars across a broad range of environments requires undertaking similar analyses in hundreds to thousands of resolved H II regions across a wide range of galactic environments (and a correspondingly large number of galaxies). As an important step in this direction, we obtained a large IFU mosaic of the nearby spiral galaxy NGC 300 (for an excellent preliminary demonstration of the capabilities of MUSE in extracting stellar spectra in crowded fields in NGC 300, see Roth et al. 2018). With a favorable inclination angle, a distance of ~ 2 Mpc (Dalcanton et al. 2009), a well-studied population of H II regions and giant molecular clouds (GMCs; e.g., Deharveng et al. 1988; Faesi et al. 2014, 2018; Kruijssen et al. 2019), and high spatial resolution, multiband *Hubble Space Telescope* (*HST*) coverage (Dalcanton et al. 2009), NGC 300 is ideally suited to showcase the power of IFU spectroscopy for deriving feedback quantities and simultaneous detailed knowledge of the massive stars driving it over a wide range of H II region properties. Our dedicated observing campaign (PI: McLeod) uses MUSE to image the central $7' \times 5'$ of the star-forming disk of NGC 300 with a 35-pointing mosaic, giving access to over 100 H II regions and their stellar content at a spatial resolution of ~ 10 pc. This type of IFU analysis of resolved H II regions will continue to grow with other ongoing and upcoming efforts (e.g., Physics at High Angular resolution in Nearby Galaxies, PHANGS, first results shown in Kreckel et al. 2018; Star formation, Ionized Gas, and Nebular Abundances Legacy Survey with SITELLE, Rousseau-Nepton et al. 2019).

In this paper, we preview our larger program and showcase the combined power of *HST*+MUSE observations of two giant H II region complexes hosting a total of five individual H II regions. For each H II region we derive integrated properties (e.g., $H\alpha$ luminosities, oxygen abundances, electron densities, and temperatures) and feedback-related pressure terms (i.e., the direct radiation pressure, the pressure from stellar winds, and the ionized gas pressure; due to the lack of X-ray emission from archival *Chandra* data, the relatively young ages of the analyzed regions, the lack of common optical supernova remnant tracers, e.g., enhanced [S II] emission with respect to $H\alpha$, and the absence of known remnants associated with the analyzed regions as per Vučićić et al. 2015, we assume that supernova events have not yet occurred); moreover, we extract spectra of the massive, feedback-driving stars in the H II regions and derive stellar atmospheric parameters by fitting Potsdam Wolf-Rayet (PoWR) model atmospheres (Hainich et al. 2019) to the detected stellar absorption lines. With the combined knowledge of the region properties and the massive stellar content, we analyze the feedback efficiency by

comparing the combined photon output from the stars to the region luminosities.

As a first comparison with similarly derived parameters, we compare our results to those described in MC19 and discuss the potential of the full 35-pointing mosaic in terms of not only obtaining integrated H II region properties (e.g., luminosities, abundances, temperatures, densities, ionized gas kinematics) over entire nearby galaxies but also determining their feedback-driving stellar content in terms of O-type and Wolf-Rayet (WR) stars. The methods and techniques will be widely applicable to similar, existing IFU data sets (e.g., PHANGS/MUSE, Kreckel et al. 2018; SIGNALS/SITELLE, Rousseau-Nepton et al. 2019) and instruments (e.g., Keck/KCWI), as well as upcoming instruments and surveys (e.g., ELT/HARMONI, SDSS-V/LVM). These will yield the necessary statistics in terms of H II region numbers and properties needed to observationally quantify stellar feedback across the wide range of physical conditions found in nearby galaxies.

This paper is organized as follows. In Section 2, we introduce the MUSE data set, discuss the data reduction, and briefly discuss the *HST* photometric catalog we used. In Section 3, we describe the stellar identification and classification process. In Section 4, we discuss the integrated properties of the five H II regions and compare the results obtained here to previous LMC feedback studies and simulations and local starburst galaxies. In Section 5, we provide an outlook for upcoming nearby galaxy IFU surveys, and we conclude in Section 6.

2. Observations and Data Reduction

2.1. MUSE IFU Data

We used the MUSE instrument (Bacon et al. 2010), mounted on the Very Large Telescope, to obtain a $7' \times 5'$ mosaic covering most of the star-forming disk of NGC 300. The data were taken in the nominal wavelength range (~ 4750 – 9350 Å) and in the instrument’s wide-field mode ($1' \times 1'$ per pointing), as part of the observing program 098.B-0193(A) (PI McLeod). These data were not taken with the adaptive optics (AO) system of MUSE, and seeing-limited angular resolutions in a range of $0''.7$ – $1''.1$ were achieved. Each pointing was observed three times in a 90° rotation dither pattern with an exposure time of 900 s per rotation. Here, we present a first analysis of the data set concerning two giant H II region complexes in the eastern part of NGC 300’s star-forming disk, covered by two of the (in total) 35 MUSE pointings of the program (shown in Figure 1), the details of which we list in Table 1. The two complexes host a total of five individual H II regions. Following the nomenclature of Deharveng et al. (1988), these are [DCL88] 118A, [DCL88]118B, [DCL88]119A, [DCL88]119B, and [DCL88]119C. Henceforth, we refer to these H II region complexes as D118 and D119 and drop the [DCL88] before the regions’ names for brevity.

The two pointings were reduced in the ESOREX environment using the MUSE pipeline (Weilbacher et al. 2012) and the standard static calibration files. For each observing block we used the available calibration files from the ESO archive for the relevant night. Standard-star calibrations were performed as part of the instrument’s pipeline, and the relevant standard-star observations¹³ (Feige 110 and EG 274 for fields 1 and 2,

¹³ See the ESO/MUSE webpages for a list of standard stars used for the instrument.

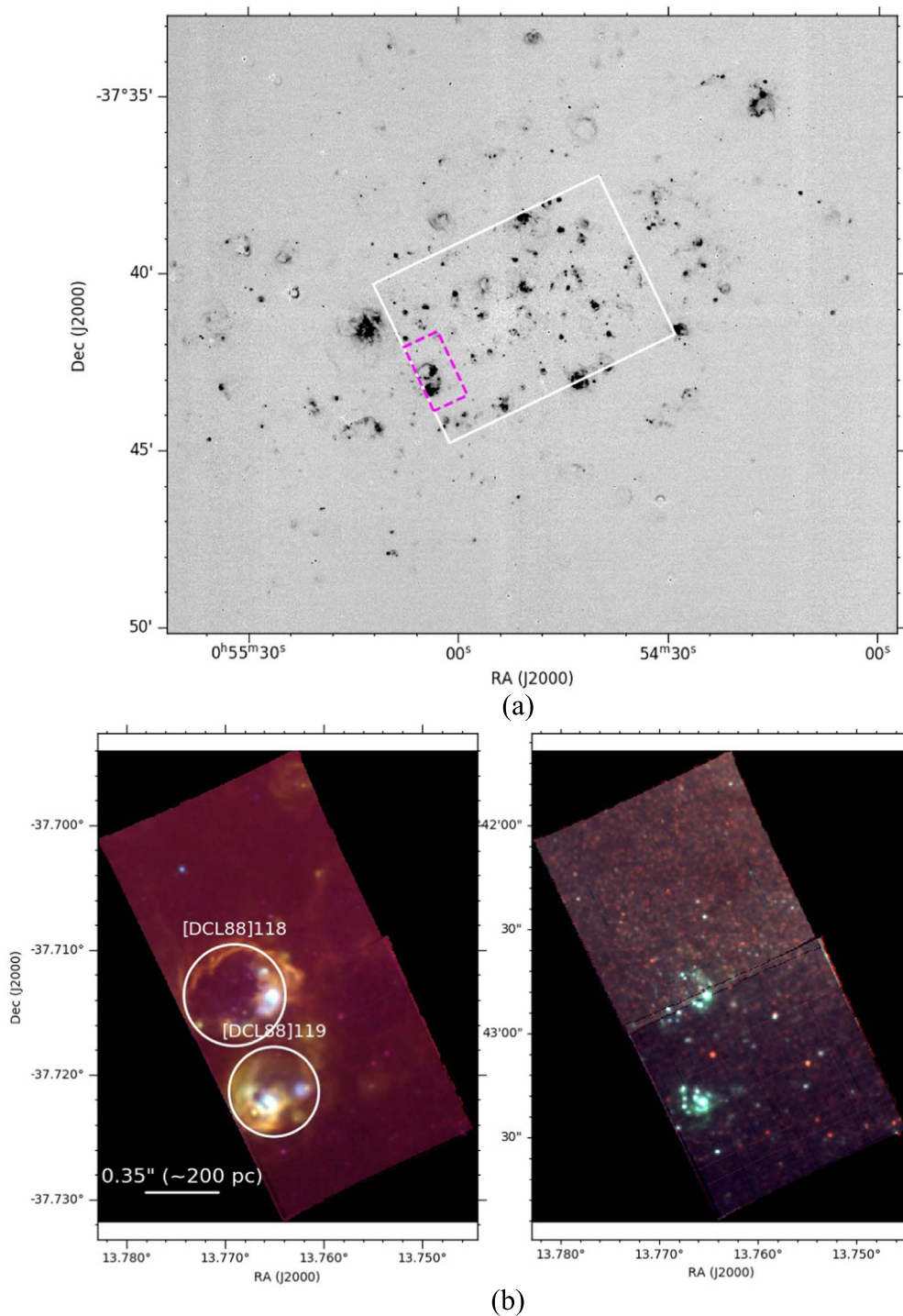


Figure 1. (a) ESO/MPG WFI $H\alpha$ image of NGC 300 (Faesi et al. 2014) showing the footprint of our $7' \times 5'$ mosaic (solid white) and the two regions analyzed here (dashed magenta). (b) Three-color composites of the two H II region complexes. Left panel: ionized gas map traced by [S II] $\lambda 6717$ (red), $H\alpha$ (green), and [O III] $\lambda 5007$ (blue); the white circles encompass 90% of the $H\alpha$ flux in each region. Right panel: arbitrary RGB (see text Section 2.1) composite highlighting the stellar population. Some nebular emission is seen in the green filter, which encompasses the $H\alpha$ line.

Table 1
MUSE IFU Observations Discussed in This Paper

Field	Field Center (J2000)	Observation Date (yyyy mm dd)	Seeing (arcsec)	t_{exp} (s)	No. of Exposures
1	00:55:04.35–37:42:19.8	2016 Nov 8	$0''.70$	900	3
2	00:55:02.15–37:43:13.5	2018 Jul 23	$\sim 1''.06$	900	3

respectively) were taken as part of the nightly MUSE calibration plan with an exposure time of 40 s. The three exposures per pointing of the two data cubes were then combined into two single cubes with the built-in exposure combination recipes of the MUSE pipeline.

Our program does not include dedicated sky offsets, but with an exposure time of 900 s the MUSE spectra are heavily contaminated by skylines. Atmospheric contamination increases toward the red part of the MUSE wavelength coverage, where many O and OH transitions occur. This is particularly problematic in terms of spectral classification of, e.g., lower-mass stars, as several crucial features (e.g., the Ca II triplet) lie within that range. Atmospheric contamination is also problematic in terms of ionized gas studies, as several nebular emission lines (e.g., the Balmer lines used for extinction measurements, the density-sensitive [S II] λ 6717, 31 doublet) are surrounded by and blended with skylines.

In the absence of dedicated sky observations, the MUSE pipeline relies on estimating the sky emission from a user-defined percentage of the darkest pixels in a given, specific data cube, and the so-created sky spectrum is then subtracted from all the spaxels (spectral pixels) in that specific cube. For observations targeting regions with strong nebular emission this method is, unfortunately, not ideal, as the atmospheric contribution is due not only to O₂ and OH transitions but also to emission from species that make up a nebular spectrum (i.e., H α , H β , and [O I]). Using the sky creation and subtraction of the pipeline therefore leads to negative nebular fluxes, as the pipeline recognizes, e.g., the Balmer and atomic oxygen lines as skylines and subtracts them. To avoid this, we proceed in removing the atmospheric skylines in the following manner (a detailed description of this method is given in Zeidler et al. 2019):

- (i) Standard sky creation: the appropriate pipeline recipe (*muse_create_sky*) is used to create a sky model by using a 0.5% fraction of the input image to be considered as sky.
- (ii) Sky continuum: the previous step produces an estimated sky continuum flux spectrum, which we now set to zero. While no continuum subtraction is performed at this point, this step is necessary, as it ensures that the fluxes of the sky emission lines are estimated correctly and that the input for the next step has the correct, pipeline-recognized header.
- (iii) Zero-flux sky creation: *muse_create_sky* is called again with the sky continuum (set to zero, as described above) obtained from the previous step.
- (iv) Skyline subtraction: the calibration file containing the list of skylines, which comes as part of the pipeline's static calibration folder, is overwritten such that all but the atmospheric molecular lines (i.e., O₂ and OH) have zero fluxes. The science reduction recipe *muse_scipost* is now run on the data cube, together with the above-created sky continuum and skyline calibrations.

The result of this procedure (which also includes a telluric correction) is shown in Figure 2, where the top panel shows the integrated spectrum of Field 2 before the skyline subtraction and the bottom panel illustrates the output of the above-described method. The unlabeled emission lines in the bottom panel are residual atomic species of no direct relevance (or contamination) for this study.

Field 2 (see Table 1) was taken during nonphotometric conditions. As a result, the three exposures of Field 2 are offset

relative to one another in flux. We estimate the relative offsets by fitting the baseline of the mean spectrum of each individual cube of Field 2, and the obtained values are integrated into the MUSE pipeline during the exposure combination step, which produces the final, combined data cube of Field 2.

Moreover, due to lunar contamination, the flux offset between the three exposures is wavelength dependent, with an increasing offset toward the bluer wavelengths. In the data this is reflected by a flux increase toward bluer wavelengths. Because the pipeline can account for constant but not for wavelength-dependent flux offsets between exposures, we do not correct for lunar contamination during data reduction. Instead, this is taken into account when producing integrated emission-line maps by performing a pixel-by-pixel continuum subtraction of the data cubes, as will be described in the following paragraph.

In this paper, we analyze both the stellar and the gaseous components of the five H II regions within the two large complexes. Both components require absorption from the galactic stellar background to be accounted for. For the stellar spectra analyzed in this work this step is necessary to disentangle intrinsic stellar absorption features from those produced by the galactic background (this will be further discussed in Section 3). In terms of the nebular analysis, the stellar galactic background introduces absorption features in the Balmer lines, which are superimposed on the emission of nebular origin and can lead to faulty line ratio values, e.g., higher H α /H β ratios, used during extinction correction. We therefore proceed in performing a pixel-by-pixel continuum subtraction and background correction. The continuum subtraction is performed by fitting and subtracting a fourth-order polynomial¹⁴ to each spaxel, followed by the subtraction of the local background. The former therefore removes both the lunar and the stellar continua simultaneously. For the background subtraction, the mean of a 3-pixel radius aperture (motivated by the point-spread function [PSF] fit described in Section 3) containing pixels representative of the darkest 5% of pixels (i.e., without nebular emission and not coinciding with stellar sources) in each cube is used for the pixel-by-pixel background subtraction. This results in a continuum- and background-subtracted data cube per field. These two cubes are then manually combined into a single, 2' \times 1' data cube, which is used to derive the integrated (nebular) properties described in Section 4.

To validate the flux offset, stellar background, and continuum subtraction corrections performed prior to data analysis, we compare the MUSE H α fluxes obtained from the MUSE H α map by integrating over the two H II region complexes (white regions in Figure 1, corresponding to the radii encompassing 90% of the H α flux; see Section 4.1) with fluxes obtained from the same apertures from ESO/WFI data¹⁵ (Faesi et al. 2014) before and after the correction. The flux comparison is listed in Table 2, showing good agreement between the WFI and corrected MUSE fluxes.

¹⁴ The high polynomial order used for the continuum fit is motivated by the large fraction of continuum in each spectrum available thanks to precise user-defined wavelength ranges to be excluded from the fit available in the PYSPECKIT package used for this.

¹⁵ The WFI H α filter has a central wavelength of 6588.27 Å and an FWHM of 74.31 Å, and therefore it also covers the [N II] lines. As described in Faesi et al. (2014), the [N II] contamination was removed and the continuum subtracted; hence, the resulting H α map is comparable to the MUSE map, which only covers the H α line.

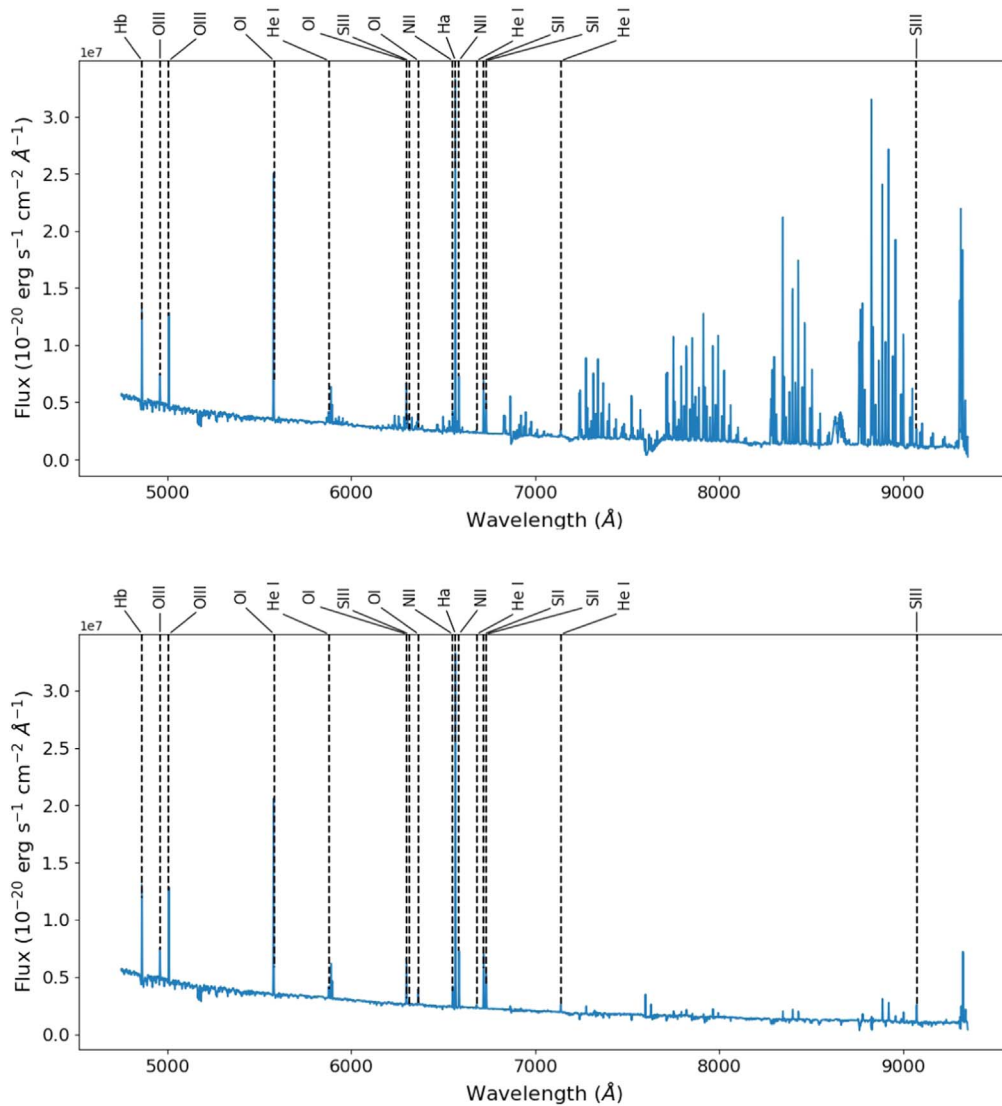


Figure 2. Integrated spectrum of Field 2 before (top panel) and after (bottom panel) sky subtraction. The main nebular emission lines are indicated (unlabeled emission lines in the bottom panel are residual atomic species of no direct relevance for this study).

Table 2

Comparison of the $H\alpha$ Fluxes Obtained from the MUSE Data Set Prior to and after Flux Offset Correction (See Section 2.1) with Archival ESO/WFI $H\alpha$ Fluxes (Faesi et al. 2014)

Region	F_{MUSE}	$F_{\text{MUSE, corr}}$	F_{WFI}
[DCL89]D118	50.61 ± 0.01	58.68 ± 0.02	60.84 ± 0.06
[DCL89]D119	75.47 ± 0.01	106.26 ± 0.01	105.69 ± 0.07

Note. WFI fluxes are obtained by performing aperture photometry on the circular regions shown in Figure 1. All fluxes are in units of 10^{-14} erg $\text{s}^{-1} \text{cm}^{-2}$ and are pre-extinction (MW + intrinsic) correction.

To show the spatial distribution of the ionized gas in relation to the ionizing, massive stars, we produce emission-line maps of the main nebular lines (by collapsing the cubes $\pm 3 \text{ \AA}$ around the central, redshifted, wavelength of each line, i.e., $H\beta$, [O III] $\lambda\lambda 4959, 5007$, [N II] $\lambda\lambda 6548, 84$, $H\alpha$, [S II] $\lambda\lambda 6717, 31$, [O II] $\lambda\lambda 7320, 30$, [S III] $\lambda 9068$). We also produced maps in three custom filters, which simply divide the spectral axis of the cube into three arbitrary ranges. For simplicity, we call these

B , G , and R ($4750\text{--}6283 \text{ \AA}$, $6284\text{--}8717 \text{ \AA}$, and $8718\text{--}9350 \text{ \AA}$, respectively). The resulting three sub-cubes are then collapsed along the spectral axis to obtain images in each filter. This is shown in Figure 1, as a nebular three-color composite image (the left panel shows $r = [\text{S II}] \lambda 6717$, $g = H\alpha$, $b = [\text{O III}] \lambda 5007$, and the corresponding RGB composite is in the right panel).

2.2. HST Photometry

As will be described in Section 3, we use high angular resolution *HST* photometry catalogs to deblend and resolve single stars and then extract their spectra from the ground-based MUSE data. NGC 300 was covered by the ACS Nearby Galaxy Survey (ANGST; Dalcanton et al. 2009) in three broadband photometric filters, i.e., F435W, F606W, and F814W. Additionally, ANGST combined these observations with archival *HST* data of NGC 300 (Butler et al. 2004; Rizzi et al. 2006), including F555W observations.

For each observed field, ANGST provides publicly available star catalogs, which contain the photometry for each object

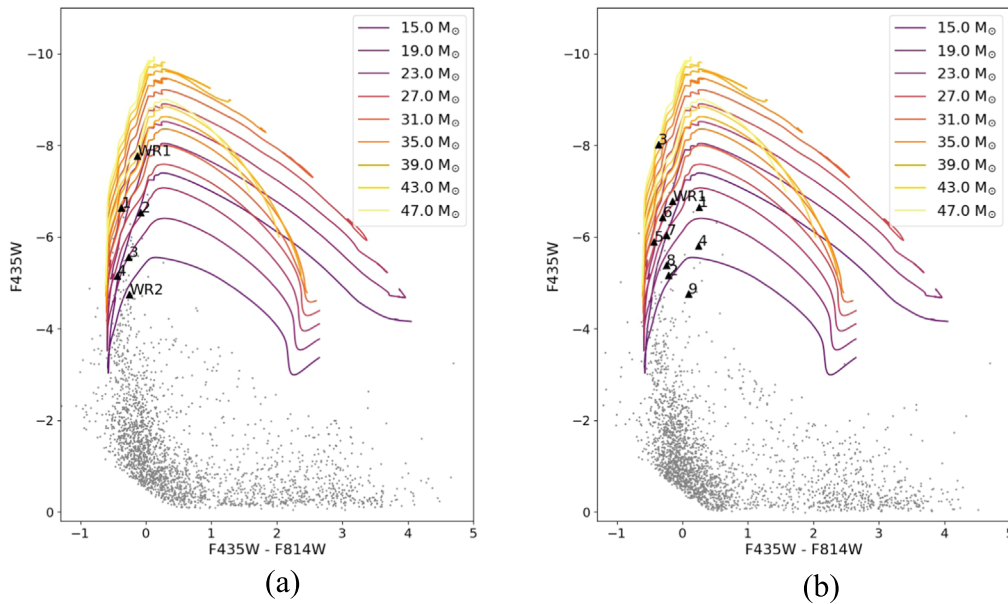


Figure 3. CMDs of D118 (left) and D119 (right) from the cropped ANGST star catalogs (within $22''$ of the cluster centers and with $S/N > 10$; gray data points; see Section 2.2) with MIST evolutionary tracks (Choi et al. 2016) (in the mass range $M = 15\text{--}47 M_{\odot}$) overlotted on both panels. The O-type and WR stars in D118 and D119 are marked with black triangles. Unlabeled bright objects in the CMDs are B-type stars not analyzed in this paper.

classified as a star and with $S/N > 4$ (we refer to Dalcanton et al. 2009 for details on photometry measurements and point-source classification). ANGST also provides “good-star” catalogs, in which additional sharpness and crowding cuts have been applied. Because of these criteria, the good-star catalog is not ideal when analyzing star clusters where stars are crowded by definition, and we therefore use the above-mentioned star files in this paper, rather than the “good-star” catalogs.

From the ANGST catalog covering the two H II region complexes (and containing a total of 373,677 sources), we extract stars within $22''$ (~ 215 pc) of the central coordinates of the H II region complexes. Given the angular sizes of D118 and D119 (which have radii of $\sim 14''_6$ and $13''$, respectively; see Figure 1), $22''$ encompasses the cluster stars and field stars that are representative of the stars in the region surrounding each star cluster. These more isolated field stars are necessary to compute the PSF, as will be described in Section 3. We further limit the *HST* catalog by selecting only bright sources, i.e., $m_{F814W} < 22$, corresponding to the *I*-band limiting magnitude of our MUSE observations, having signal-to-noise ratio (S/N) > 10 in both filters (F435W and F814W). This results in two catalogs with 76 and 69 stars for D118 and D119, respectively. Typical photometric errors of ANGST magnitudes are of the order of $\sim 10^{-3}$.

Figure 3 shows *HST* color–magnitude diagrams (CMDs) for $22''$ apertures around the central coordinates of the two H II region complexes, assuming a distance modulus of 26.5 for NGC 300 (corresponding to a distance of 2 Mpc to NGC 300; Dalcanton et al. 2009). For completeness, in Figure 3 we show all stars, i.e., including those with $m_{F814W} > 22$, within $22''$ of the cluster centers (2313 and 2384 stars for D118 and D119, respectively). Overplotted are MIST¹⁶ evolutionary tracks (Choi et al. 2016; Dotter 2016) in the mass range $M = 15\text{--}47 M_{\odot}$ (in steps of $4 M_{\odot}$) for $[\text{Fe}/\text{H}] = -0.5$ (Richer et al. 1985) and with $A_V = 0.06$ (Burstein & Heiles 1984).

¹⁶ MESA Isochrones & Stellar Tracks (<http://waps.cfa.harvard.edu/MIST/>).

3. Stellar Spectroscopy and Classification

At the distance of NGC 300, the seeing-limited spatial resolution of MUSE results in blending of single stellar sources in crowded regions, e.g., star clusters (see Section 3.1.9). To extract stellar spectra from these regions and study their stellar content, we exploit the PYTHON package PAMPELMUSE (Kamann et al. 2013) to compute a wavelength-dependent PSF for the stellar sources in our MUSE cubes. As described in Zeidler et al. (2018), PAMPELMUSE performs PSF photometry of isolated bright sources in an IFU cube based on a high angular resolution photometric catalog. If run to full completion, after the PSF fit (which also includes a WCS correction between the input catalog and the corresponding sources detected in the IFU data), PAMPELMUSE then propagates the PSF profile to all the stellar sources listed in the input catalog, estimates and subtracts the background around each star, and finally delivers a spectral catalog of all identified sources.

Given that the current version of PAMPELMUSE is not designed to perform background estimates for stars within H II regions, we are not able to use the output spectra, as the heavy contamination by nebular emission lines results in a faulty background subtraction. We therefore only use PAMPELMUSE to perform its first analysis stage, i.e., the PSF fit and WCS correction.

We then perform a first spectroscopic analysis to identify the massive, feedback-driving stars¹⁷ within the H II regions by evaluating the presence (or absence) of specific spectral lines characteristic of O-type and WR stars:

1. O-type stars: He II $\lambda 5411$, He I $\lambda\lambda 4921, 5876, 6678, 7065, 7281$;
2. WR stars: broad He II $\lambda 5411$ and He I $\lambda\lambda 4921, 5876, 6678, 7065, 7281$ emission, C III $\lambda 5696$ and C IV $\lambda 5808$ (WC stars), N III $\lambda 8237$ (WN stars), O V $\lambda 5835$ (WO stars).

¹⁷ This study focuses on massive stars, as these dominate over intermediate- and low-mass stars in terms of feedback energetics. We will discuss the extraction and classification of all stars down to the detection limit within these two regions in a forthcoming publication.

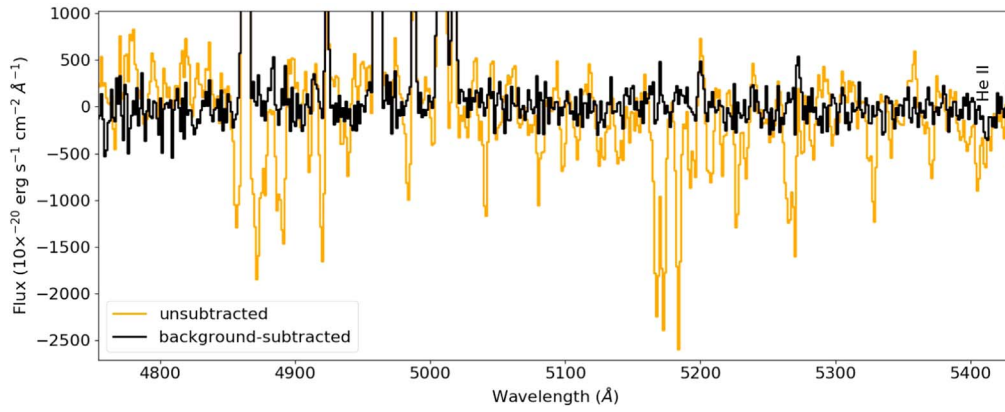


Figure 4. Continuum-subtracted spectrum of the O-type star [DCL89]119-5 before (orange) and after (black) correcting for the unresolved galactic stellar background. The location of the He II $\lambda 5411$ line, used to classify O stars, is indicated. Given the large wavelength range covered by MUSE ($\sim 4750\text{--}9350$ Å), we cropped the shown spectrum to a smaller (yet representative) portion to better illustrate the result of the galactic background subtraction. The level of noise in the continuum of the background spectrum is ≈ 60 .

To evaluate the presence (or absence) of spectral lines, we crop the extracted spectra to ± 50 Å around the central wavelength of each line and perform a continuum fit and subtraction. Ideally, the detection and significance of a line should be quantified by evaluating the presence of data points above a certain noise threshold. However, given that the stars of interest are embedded in H II regions and superimposed on a galactic background, their spectra are noisy. To ensure that the above criteria do not lead to false negatives (and hence to an underestimate of the combined energy input of the massive stellar populations in the regions), we visually inspect each line to confirm its significance. Moreover, we require the following conditions to be satisfied: (i) the width of the line has to be > 1.25 Å (i.e., greater than the spectral sampling of MUSE), and (ii) we require the fitted line centroid to be within 2 times the spectral sampling (e.g., 5413.3 ± 2.5 Å). Corresponding to a velocity of ~ 140 km s $^{-1}$, the latter assumes that the H II regions are young and that the stars are still associated with the surrounding gas, which is reasonable considering that the systemic velocities of D118 and D119 are ~ 102 and ~ 105 km s $^{-1}$, respectively (derived from VLA H I data; Faesi et al. 2014). This also ensures that potential OB runaways with velocities up to ~ 40 km s $^{-1}$ are not missed (e.g., Gies & Bolton 1986).

The resulting stellar spectra are subsequently corrected for the unresolved galactic stellar background, which introduces absorption features of an old stellar population in the spectra of our young, massive stars of interest. The galactic stellar background is estimated from the integrated spectrum of an aperture centered on a dark pixel (from the darkest 5% of pixels from each cube, i.e., without nebular emission and not coinciding with stellar sources, as was used for the nebular emission analysis). Because the stellar background is unresolved across the entire field of view, the dark region can be taken as representative for the background subtraction. The background aperture is equal in size to the PSF-fitted aperture used to extract stellar spectra; hence, we subtract a background spectrum integrated over the same number of pixels. Figure 4 shows the result of the stellar background correction of the O-type star [DCL89]119-5 (see Section 3.1.9): the uncorrected spectrum (orange) shows deep absorption features from the older galactic population along the line of sight, which lead to

Balmer absorption and contamination of absorption lines relevant for spectral classification such as the He II $\lambda 5411$ line.

In MC19 we use MUSE data to classify O-type stars in H II regions in the LMC based on the equivalent width (EW) of the helium lines (e.g., Kerton et al. 1999). This empirical method of determining the spectral type of massive, O-type stars relies on the EW ratio of the atomic and singly ionized He absorption lines, e.g., $EW_{\lambda 4921}/EW_{\lambda 5411}$. Due to the stars being embedded in the ionized material of the H II regions, the He I $\lambda 4921$ line is unreliable for spectral typing, as it can be of nebular origin when in emission (e.g., Byler et al. 2018), therefore contaminating the potential stellar absorption line. Instead, we derive atmospheric parameters by fitting the He II $\lambda 5411$ absorption line with PoWR model atmospheres (Hainich et al. 2019). The PoWR grids come in Galactic, LMC, and SMC metallicities for both WR and O-type stars. With $Z \approx 0.33 Z_{\odot}$ for NGC 300 (Butler et al. 2004), we use the PoWR LMC model atmospheres ($Z = 0.5 Z_{\odot}$), which are closest in metallicity to NCG 300 (see, e.g., Ramachandran et al. 2018, 2019 for an application of PoWR models in the Magellanic Clouds). We crop the modeled and the observed spectra of the identified O-type stars to a wavelength range of 5380–5440 Å and find the best-fit model for each star via χ^2 minimization,

$$\chi^2 = \sum_{i=1}^N \frac{(O_i - E_i)^2}{\sigma_i}, \quad (1)$$

with O being the observed flux, E the model flux, and σ the mean noise of the spectrum plus a random (Gaussian) noise component equivalent to the computed noise, and we use a Monte Carlo approach (for each star we perform 1000 runs) to estimate the 1σ errors on the fitted parameters. For the ionizing photon fluxes associated with each grid model, as well as the WR luminosities (for which constant mass and luminosity is assumed throughout the PoWR grid models), we adopt a generous 20% uncertainty.

In terms of stellar feedback, the main stellar parameter of interest for this work derived from the PoWR model atmosphere fit are the bolometric luminosities of the stars, as well as the amount of ionizing (Lyman continuum) photons emitted per second, Q_H (Columns (4) and (7) in Table 3). In this respect, there are three major sources of uncertainty that we

Table 3
Model Stellar Parameters for the O-type Stars Reported from the Best-fit PoWR Atmospheres (Hainich et al. 2019) (with Column (3) Indicating the Best-fit Model Name)

ID	Coordinates (J2000)	PoWR Model	$\log L$ (L_{\odot})	$\log T_{\text{eff}}$ (K)	$\log g$ (cgs)	$\log Q_{\text{H}}$ (s^{-1})	M (M_{\odot})	M_{MIST} (M_{\odot})
[DCL88]118-1	0:55:03.63–37:42:49.05	30–36	5.0 ± 4.4	4.48 ± 3.57	3.6 ± 0.3	48.08 ± 47.61	21.5 ± 0.8	23
[DCL88]118-2	0:55:04.24–37:42:43.06	28–34	5.1 ± 4.2	4.45 ± 3.60	3.4 ± 0.4	47.98 ± 47.58	23.0 ± 0.7	24
[DCL88]118-3	0:55:03.61–37:42:48.46	31–38	4.8 ± 4.3	4.49 ± 3.67	3.6 ± 0.3	47.92 ± 47.45	18.8 ± 1.2	19
[DCL88]118-4	0:55:03.84–37:42:43.12	28–30	5.9 ± 5.3	4.47 ± 3.35	3.0 ± 0.2	49.15 ± 48.44	49.2 ± 9.6	17
[DCL88]119-1	0:55:03.85–37:43:16.68	30–36	5.0 ± 4.9	4.48 ± 3.36	3.6 ± 0.3	48.08 ± 47.38	21.5 ± 8.1	20
[DCL88]119-2	0:55:03.84–37:43:23.43	44–40	5.6 ± 4.8	4.64 ± 3.47	4.0 ± 0.2	49.41 ± 48.60	47.5 ± 4.1	16
[DCL88]119-3	0:55:03.73–37:43:19.93	33–44	4.3 ± 4.2	4.52 ± 3.28	4.4 ± 0.3	47.38 ± 47.06	15.7 ± 4.6	43
[DCL88]119-3 ^a	...	33–34	5.7 ± 5.3	4.52 ± 3.82	3.4 ± 0.7	49.21 ± 48.51	41.3 ± 8.3	43
[DCL88]119-4	0:55:03.70–37:43:19.42	33–42	4.5 ± 3.9	4.52 ± 3.28	4.2 ± 0.3	47.70 ± 47.25	17.2 ± 5.4	16
[DCL88]119-5	0:55:03.67–37:43:21.53	36–42	4.8 ± 4.3	4.56 ± 3.50	4.2 ± 0.3	48.21 ± 47.67	21.6 ± 8.6	19
[DCL88]119-6	0:55:03.73–37:43:19.79	31–38	4.8 ± 4.4	4.49 ± 3.03	3.8 ± 0.3	47.92 ± 47.29	18.8 ± 3.9	19
[DCL88]119-7	0:55:04.28–37:43:15.83	33–44	4.3 ± 4.2	4.52 ± 3.29	4.4 ± 0.4	47.38 ± 46.56	15.7 ± 6.8	15
[DCL88]119-8	0:55:03.78–37:43:18.91	33–44	4.3 ± 3.7	4.52 ± 3.29	4.4 ± 0.3	47.38 ± 46.00	15.7 ± 4.8	16
[DCL88]119-9	0:55:03.77–37:43:18.73	33–42	4.5 ± 3.5	4.52 ± 3.23	4.2 ± 0.3	47.70 ± 47.96	17.2 ± 5.3	< 15

Notes. The last column lists approximate stellar masses as derived (by eye) from the CMD. The fitted spectra are shown in Figures 6 and 7. Uncertainties on the fitted parameters correspond to the 1σ standard deviation from 1000 Monte Carlo runs.

^a Revised parameters of 119-3 obtained by additionally fitting the He II $\lambda 6406$ line; see Section 3.1.8.

briefly discuss here. First, we note wind contamination of the He II $\lambda 5411$ line: this is mainly problematic in the case of extreme supergiants, which we do not observe in the two regions. Second, we do not account for unresolved binaries, and the derived photon fluxes are therefore lower limits. Third, in a $\sim 20 \text{ \AA}$ proximity of the He II $\lambda 5411$ line, there are several metal lines from the galactic background, the subtraction of which is a potential source of uncertainty (i.e., by decreasing the amplitude of the He II line). In the background subtraction illustrated in Figure 4, the S/N of the He II line at 5411 \AA improves from ~ 1.1 before to ~ 2.2 after the background correction, showing that over-subtraction is not problematic. We furthermore note that the He II $\lambda 5411$ absorption line is not surrounded by (or blended with) any nebular emission line; hence, we do not expect the nebulosity to affect the stellar classification.

However, the main problem in deriving the stellar parameters is the uniqueness of fitting: for an observed depth of the He II absorption line there is a suite of models from the grid with different sets of surface gravity, mass, and temperature that fit (see the Appendix, Figure 15). In addition to the χ^2 minimization, in the next sections we therefore evaluate the validity of obtaining stellar parameters from the PoWR model fits by comparing the effective temperatures and luminosities (see Table 3) derived from the PoWR models with those obtained (by eye) from the *HST* CMD (see Figure 3). The combination of the MUSE spectroscopy and the *HST* photometry therefore allows us to reliably derive stellar parameters. In the feedback analysis presented in Section 4, we proceed in combining photon flux and luminosity of the single stars to summed fluxes and luminosities in each region (depending on their stellar content), and we will discuss the uncertainty on the combined parameter flux at that stage.

Spectral contamination by nebular emission lines becomes an issue when fitting PoWR models to the WR spectra, as the classification of these relies on the (broad) emission features characteristic for these kinds of stars. The nebular contamination is in the form of narrow emission lines superimposed on the broad WR lines, and we remove these prior to

classification by fitting two-component Gaussians to the emission features and subsequently removing the narrow (nebular) component.

3.1. Stars in the D118 and D119 Complexes

In the two complexes analyzed, the classification results in the identification of 13 O-type stars (4 in the D118 complex and 9 in D119), and 4 WR stars (2 in D118 and 2 in D119). Two of the WR stars have been previously identified (Breysacher et al. 1997; Schild et al. 2003), validating our classification process. Of the 13 O-type stars, none were previously known (e.g., Bresolin et al. 2002), making these first detections and classifications. The coordinates and best-fit PoWR model parameters are listed in Tables 3 and 4. The last column in Table 3 also lists the approximate ($\pm 3 M_{\odot}$) mass for each star as derived from the MIST evolutionary tracks shown in Figure 3.

Figure 5 shows the spatial distribution of the identified O and WR stars relative to the H II region complexes, as shown by ionized gas emission (left) and stellar RGB (right). The top row of Figure 5 shows the D118 complex, which includes two H II regions (118A, 118B; highlighted with white circles). The ionized gas emission reveals a large (~ 140 pc) bubble from the center of which no gaseous emission is detected, a thin rim mainly seen in [S II] emission (see Figure 1), and a higher-ionized region to its southwest. It is in the center of this highly ionized region that the O and WR stars are found, mostly spatially coincident with the individual H II regions 118A and 118B. The spectra of the identified massive stars (cropped to the relevant He II absorption line) are shown in Figure 6, together with the best-fit PoWR models (magenta). We note that there are at least four candidate O-type stars in D118, but no reliable fit could be obtained, because He II $\lambda 5411$ emission is superimposed on the stellar absorption. We therefore do not include these in the analysis.

The bottom panels of Figure 5 show the three H II regions in the D119 complex (i.e., 119A; 119B; 119C; white circles). As for D118, no O-type stars are found in the literature for this H II

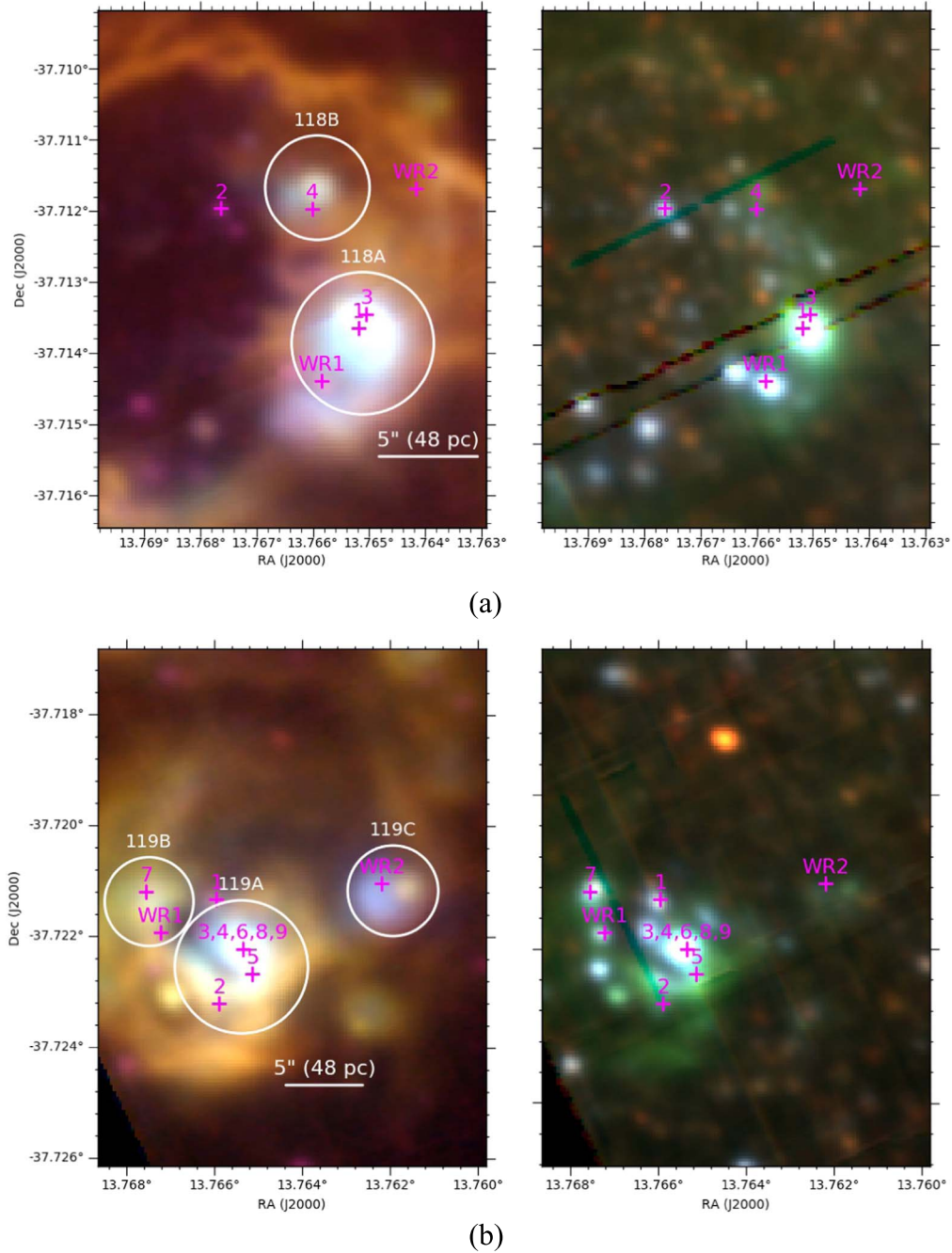


Figure 5. (a) [DCL88]118 and (b) [DCL88]119 zoom-ins showing the location of the identified O-type and WR stars (magenta plus signs). The false-color composites in both panels are the same as in Figure 1 (on the left, red: [S II] $\lambda 6717$; green: H α ; blue: [O III] $\lambda 5007$; on the right, arbitrary RGB). White circles indicate the five individual H II regions within the D118 and D119 complexes. In panel (b) sources 119-3, 4, 5, 6, 8, and 9 are marked by a single plus sign; a zoomed-in version of this image is shown in Figure 9. Image artifacts (e.g., top right panel) are due to mosaicking and do not affect the analysis.

Table 4
Wolf-Rayet Stars

ID	Coordinates (J2000)	PoWR Model ^a	$\log L$ (L_{\odot})	$\log T_{\text{eff}}$ (K)	$\log Q_{\text{H}}$ (s^{-1})	\dot{M} ($M_{\odot} \text{ yr}^{-1}$)	Type
[DCL88]118-WR1	0:55:03.78–37:42:51.80	...	5.6 ^b	...	49.50 ^b	...	early WC
[DCL88]118-WR2	0:55:03.41–37:42:42.14	09–10	5.3	4.90	49.18	–5.39	WC7
[DCL88]119-WR1	0:55:04.17–37:43:18.91	06–13	5.3	4.65	49.10	–4.79	WN8
[DCL88]119-WR2	0:55:02.94–37:43:15.96	...	5.6 ^b	...	49.50 ^b	...	early WC

Notes.

^a Hainich et al. (2019).

^b Sources 118-WR1 and 119-WR2 do not have best-fit PoWR models; the ionizing photon flux is an assumption (see text Section 3).

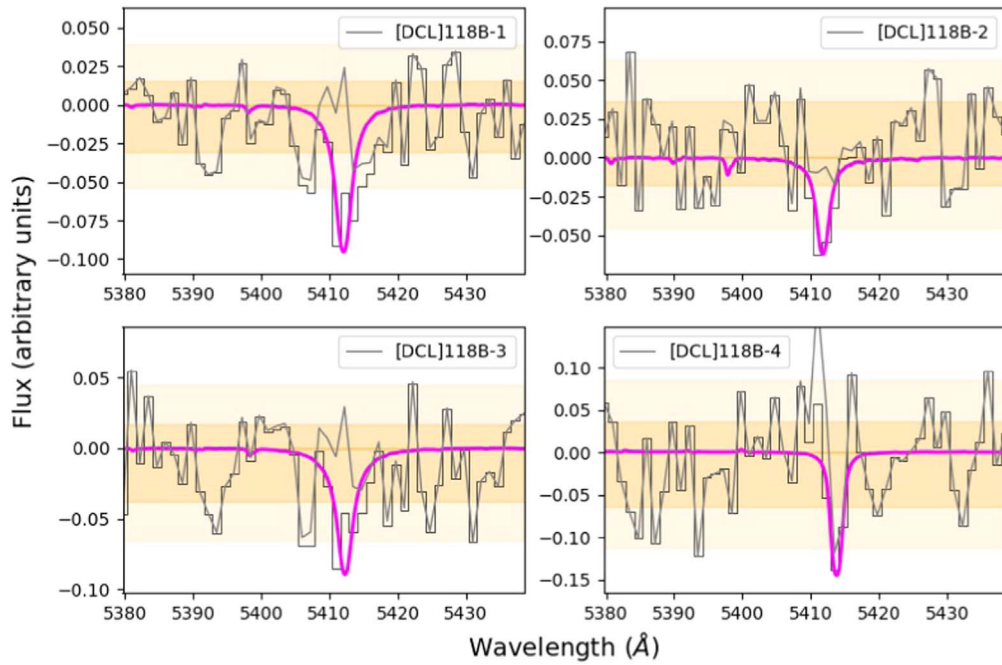


Figure 6. He II $\lambda 5411$ line of the four D118 O-type stars (black), the best-fit PoWR model atmosphere (magenta), and residuals (gray). See Section 3 and Table 3 for details.

region complex, while there are two WR stars, one confirmed and one candidate (sources #38 and #33 in Schild et al. 2003, respectively). From the presence of the He II $\lambda 5411$ absorption line we identify five O-type stars within D119 (see Table 3). The spectra of the D119 O-type stars are shown in Figure 7, together with the best-fit PoWR model atmospheres (magenta). We find two candidate O-type stars that show He I in absorption but either have contaminated He II absorption lines or lack reliable ones altogether, and are therefore not included in the analysis of this paper.

In the following, we discuss the classification of the individual sources in each region.

3.1.1. [DCL88]118-1

With an absolute magnitude of $M_{F435W} = -6.63$, this source is among the brightest in 118A, and it is associated with bright [O III] $\lambda 5007$ emission (see Figure 5). On the CMD it is identified as either a young, massive ($\sim 33 M_{\odot}$, $\log(L/L_{\odot}) \approx 5.2$) star or an older (~ 8 Myr) and less massive ($\sim 23 M_{\odot}$, $\log(L/L_{\odot}) \approx 5.3$) star. PoWR model fitting yields a mass of $21.5 M_{\odot}$ and a luminosity of $\log(L/L_{\odot}) \sim 5.0$, hence favoring the less massive MIST track, and also consistent with an age of ~ 4 Myr reported by Faesi et al. (2014).

3.1.2. [DCL88]118-2

Located further inside the main bubble of the D118 complex than the other O-type stars identified in this region, the model atmosphere fit of 118-2 is consistent with the stellar parameters derived from the CMD, i.e., consistent with a luminous $\sim 23 M_{\odot}$ star.

3.1.3. [DCL88]118-3

In the MUSE data, 118-3 and 118-1 are blended into one luminous source in the 118A region on the southwestern rim of

the giant D118 bubble. Given the high spatial resolution *HST* input catalog, we are able to deblend the two stars (with a separation of approximately 20 times the spatial resolution of *HST*/ACS, and F435W and F814W S/Ns of 249.8 and 332.9, respectively, these are therefore clearly two distinct stars) and obtain separate stellar parameters. We find, in agreement with the *HST* photometry, that 118-3 is a $\sim 18.8 M_{\odot}$ star with a luminosity of $\log(L/L_{\odot}) \sim 4.9$.

3.1.4. [DCL88]118-4

From the model atmosphere fitting routine, this O-type star appears to be the most massive source in the D118 complex. However, this is not reflected in the CMD, where 118-4 appears to be less luminous than the other three O-type stars in the region and is more consistent with MIST tracks in the 19–23 M_{\odot} range, rather than the 49.2 M_{\odot} mass derived from the model fit. Given an extinction of $A_V \sim 0.5$ (from the MUSE H β and H α lines) in that region and the fact that this star has formed its own small bubble of highly ionized gas in the form of [O III] $\lambda 5007$ emission (see top left panel of Figure 5), we suggest that this is indeed a high-mass source as obtained from the PoWR model fitting, and therefore we adopt the derived photon flux for the feedback analysis discussed in Section 4.

3.1.5. [DCL88]118-WR1 and [DCL88]118-WR2

Both of the D118 WR stars, 118-WR1 and 118-WR2, are listed in Schild et al. (2003) (their sources #37 and #34, respectively), and while 118-WR2 is classified as a WC5–6 star in that study, 118-WR1 is listed as a candidate WR star. MUSE spectra for these two sources are shown in Figures 10 (panel (a)) and 11 (black spectrum), respectively. We fit the spectrum of 118-WR2 to the WC PoWR grid and obtain a temperature of $T \sim 79.4$ kK and a luminosity of

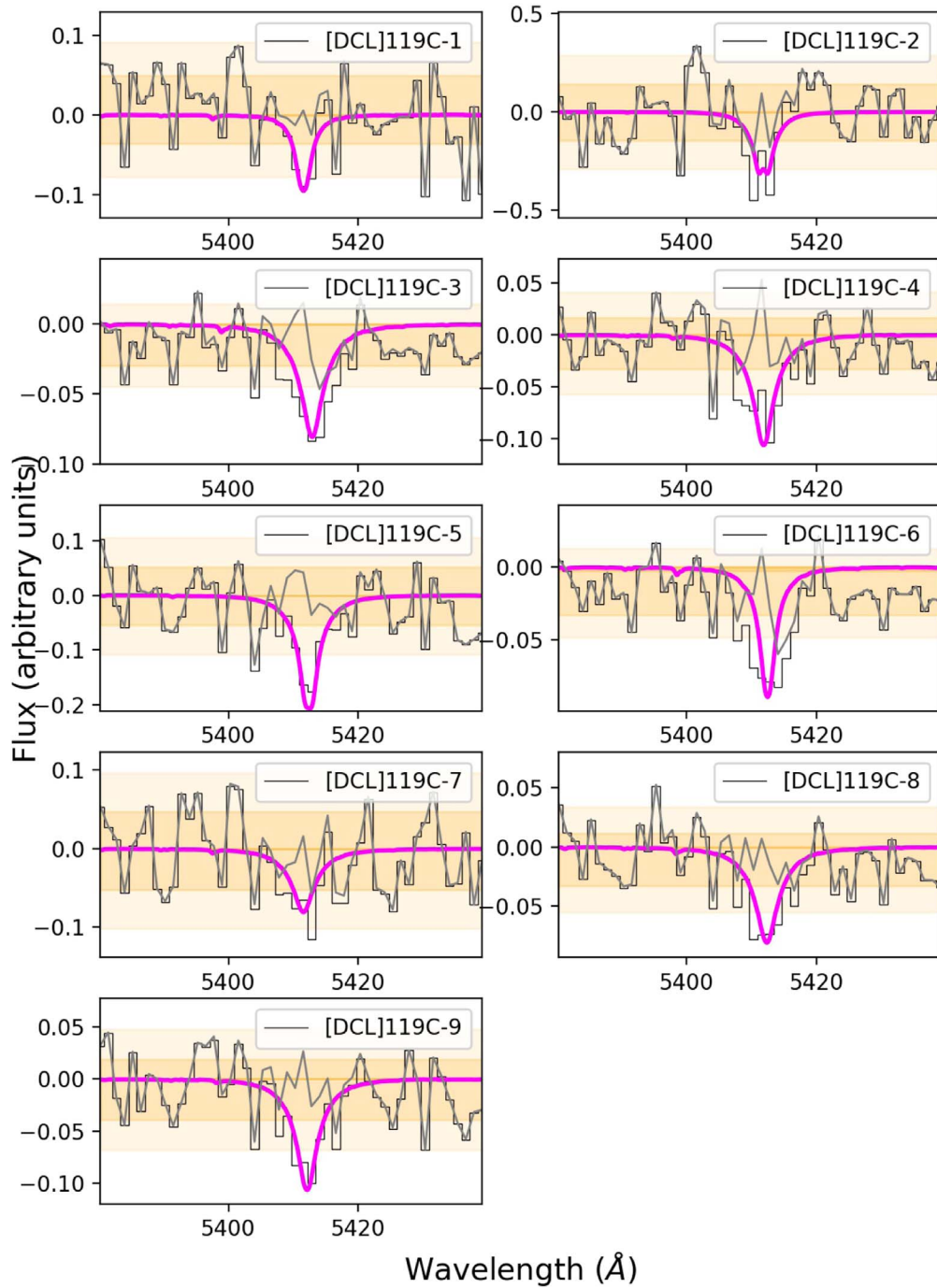


Figure 7. He II $\lambda 5411$ line of the nine O-type stars in D119 (black), the best-fit PoWR model atmosphere (magenta), and residuals (gray). See Section 3 and Table 3 for details.

$\log(L/L_{\odot}) = 5.3$, which are more consistent with a WC7 spectral type than with a WC5–6 type (Crowther 2007).

118-WR1 shows a dominant C IV feature at 5800 \AA , and aside from some possible Fe III absorption in the $5900\text{--}6000 \text{ \AA}$ range, there are no other WR emission features. Like 119-WR2 (see Section 3.1.10), due to the absence of O V $\lambda 5590$, C III $\lambda 5696$, and He II $\lambda 5411$ emission, we suggest that this star is an early (e.g., WC4) WC star (Gray & Corbally 2009), and therefore we assume an ionizing photon flux of $\log Q_{\text{H}} = 49.50$ and a luminosity $\log(L/L_{\odot}) = 5.6$ (Crowther et al. 2002; Crowther 2007) for our feedback analyses.

3.1.6. [DCL88]119-1

Compared to the other sources, 119-1 suffers the least from nebular contamination. From the best-fit PoWR model we find a mass of $21.5 M_{\odot}$, which is in good agreement with a tentative mass of $20 M_{\odot}$ obtained from the *HST* CMD.

3.1.7. [DCL88]119-2

The spectrum of 119-2 shows emission superimposed on the He II absorption line, indicating possible nebular contamination. Indeed, the best-fit PoWR model yields a stellar mass that

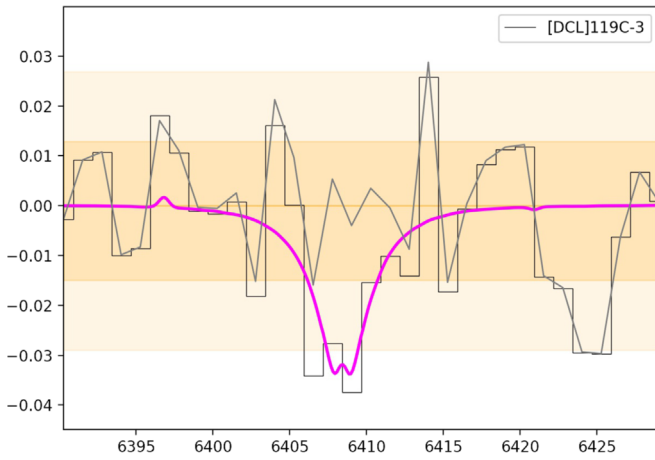


Figure 8. He II $\lambda 6406$ line of the O-type star [DCL88]119-3, the best-fit PoWR model (magenta), and the residuals (gray). See Section 3.1.8.

is almost three times what is derived from the MIST evolutionary tracks.

3.1.8. [DCL88]119-3 and [DCL88]119-4

These two stars are located in the region with the highest degree of ionization, traced by strong [O III] $\lambda 5007$ emission, and are most likely the main ionizing sources of the H II region. The PoWR mass derived for 119-4 is in good agreement with the MIST mass as per the CMD. However, for 119-3, the mass derived from the model atmosphere fit is clearly underestimated, given that the derived parameters would place 119-3 approximately 5 mag fainter on the CMD. To further investigate the stellar parameters of 119-3, we evaluate the presence of He II absorption lines redder than the $\lambda 5411$ line,¹⁸ as these become prominent for masses $\gtrsim 15 M_{\odot}$. Of these, only the He II $\lambda 6406$ line is isolated enough from nebular emission lines to guarantee a good fit. The best-fit PoWR model to the He II $\lambda 6406$ line (shown in Figure 8 and listed in Table 3) yields a mass of $M = 41.3 M_{\odot}$ and a luminosity of $\log(L/L_{\odot}) = 5.2$, which are in good agreement with the *HST* photometry.

3.1.9. [DCL88]119-5 to [DCL88]119-9

These O-type stars are all in the lower mass range ($15 M_{\odot} < M < 20 M_{\odot}$), and the PoWR model masses and luminosities are in agreement with the stars' location on the CMD. While 119-7 is located in the 119B H II region, 119-6, 8, and 9 are located in 119A, together with the stars 119-3 and 119-4, in what appears to be the brightest region of the D119 complex. This crowded region, better visible in Figure 9, is of particular importance for this work: the fact that we can deblend the stars in this region despite the insufficient spatial resolution of the MUSE data by combining it with the high angular resolution *HST* catalog demonstrates the true power of this method in extracting and classifying spectra at distances of a few megaparsecs from ground-based IFU data. Moreover, it also allows for robust spectroscopic modeling of WR stars, which are generally identified photometrically at these distances (see Section 5.1).

¹⁸ [DCL88]119-3 is the only O star in our sample showing He II lines other than the $\lambda 5411$ line.

3.1.10. [DCL88]119-WR1 and [DCL88]119-WR2

With the MUSE data we confirm two WR stars in D119. 119-WR1 (Figure 10), previously identified (Schild & Testor 1992; Breysacher et al. 1997; Schild et al. 2003) and classified as a WN9–10 star in Schild et al. (2003) (source #38 in their table 1), shows strong H, He I, and He II emission, as well as [N III]. The best-fit H-rich PoWR model yields a luminosity of $\log(L/L_{\odot}) = 5.3$, $T = 44,700$ K, and a mass-loss rate of $-4.79 M_{\odot} \text{ yr}^{-1}$, consistent with a WN8 star with a massive ($> 65 M_{\odot}$) progenitor (Crowther 2007).

119-WR2, a WR candidate in Schild et al. (2003; their source #33), is located ~ 0.2 (~ 116 pc) northwest of the approximate center of the main bubble and is associated with highly ionized ([O III]) gas; see Figure 5. Except for the C IV bump at ~ 5800 Å, the spectrum of the WC star 119C-WR2 (see Figure 11) does not show any other strong WC feature, e.g., O V $\lambda 5590$, C III $\lambda 5696$, and He II $\lambda 5411$, which would indicate WC5 and later stars (Gray & Corbally 2009). We suggest that this star is therefore likely an early (e.g., WC4) WC star and assume an ionizing photon flux of $\log Q_{\text{H}}/\text{s}^{-1} = 49.50$ and a luminosity $\log(L/L_{\odot}) = 5.6$ (Crowther et al. 2002; Crowther 2007) for our feedback analyses. We note, however, that for 119-WR2, as well as for 118-WR1, bluer spectroscopy would be required to cover the strong C III and C IV bump at 4650 Å, which would allow a PoWR model fit.

4. Integrated Properties and Stellar Feedback

With knowledge of the massive stellar content of the five H II regions in D118 and D119, we now proceed to link the feedback-driving stars to the feedback-driven gas within the regions. As mentioned in Section 1, significant progress in the field of stellar feedback can only be obtained if a large enough sample of H II regions and their stellar contents is available, such that feedback can be analyzed over a meaningful dynamic range of H II region properties and massive stars. Based on the five H II regions discussed here, in this work we develop the necessary analysis tools and methods, which can then be applied to large IFU data sets (see Section 5).

Our analysis follows MC19, where we derived a detailed census of the massive stellar populations and feedback-related quantities for a total of 11 individual H II regions in the LMC. We then compare feedback properties derived with the same methodology across the LMC and NGC 300 environments that differ in terms of metallicity, galactic host, and stellar population.

For example, in MC19 we find that by translating the spectral type of the O stars to an ionizing photon flux, $Q_{0,*}$, and relating this to the observed H α luminosity, $L_{\text{H}\alpha}$, of each region, it appears that the massive stars in the LMC are less efficient at producing the observed $L_{\text{H}\alpha}$ than prescribed by the typical case B recombination relation generally assumed for Galactic and extragalactic observations. In MC19 we suggest that a possible explanation for this discrepancy between $Q_{0,*}$ and $Q_{\text{H}\alpha}$ is a consequence of *photon leakage*, i.e., a measurable fraction of ionizing photons emitted by the massive stars that escape from the regions, and instead of contributing to the heating and ionization budget of the H II regions, they escape and contribute to the overall energetics of the host galaxy. As a result, the “feedback efficiency” describing the fraction of energy and momentum imparted on the surrounding interstellar medium (ISM) is considerably smaller than unity. However, from the LMC study alone it is not clear whether this is possibly related to the low-metallicity environment of the

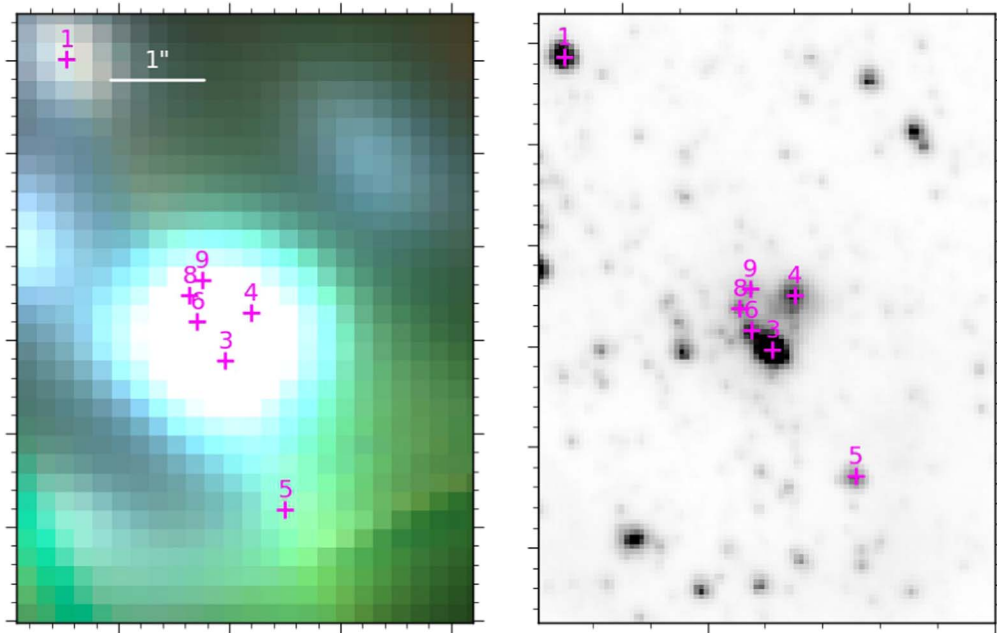


Figure 9. Zoom-in of the center of 119A illustrating the effect of lower spatial resolution of the MUSE data. The left panel is a MUSE *VRI* false-color image (see Section 2.1, resolution $\sim 1''/0$), while the right panel shows the corresponding *HST* F814W image ($\sim 0''.13$ pixel $^{-1}$ spatial resolution) from the ANGST survey (Dalcanton et al. 2009). Magenta plus signs correspond to O-type stars identified in this work (see Section 3).

LMC, motivating a comparison of regions with different metallicities (e.g., MW, LMC, SMC, NGC 300) as performed here.

4.1. Physical H II Region Parameters

As in MC19, we derive H II region radii from the radial profiles of the continuum-subtracted MUSE $H\alpha$ maps, so that R_{90} is the radius that encompasses 90% of the $H\alpha$ flux (see Appendix A.3). Given the different morphological appearances of the various H II regions, this phenomenologically defined radius ensures that uncertainties between regions are mitigated (e.g., Lopez et al. 2014). We use the derived radii to extract the corresponding integrated spectrum for each region, and we measure emission-line intensities from Gaussian fits to the main nebular lines. The emission-line fluxes are corrected for (intrinsic) extinction with the reddening correction routine of PYNEB (Luridiana et al. 2015), assuming $R_V = 3.1$ and a Galactic extinction curve (Cardelli et al. 1989). The extinction-corrected line fluxes are then used to derive electron densities and temperatures (from the [N II] and [S II] lines, respectively, as in McLeod et al. 2015). All physical parameters described in this section are listed in Table 5.

Overall, we find electron temperatures of the order of 10^4 K, as well as low electron densities, i.e., $n_e < 100$ cm $^{-3}$. We compare the quantities derived for 118A to values from Toribio San Cipriano et al. (2016), who use optical spectroscopy to derive C and O abundances for seven regions in NGC 300. With their region R23 corresponding to a small ($5''.4 \times 3''$) region around the O stars 118-1 and 118-3, we find good agreement between their electron density and temperature and those derived in this work. Specifically, these are $n_e = 70 \pm 8$ cm $^{-3}$ and $T_e = 9586 \pm 257$ K versus $n_e < 100$ cm $^{-3}$ and $T_e = 8570 \pm 1300$ K for this work and Toribio San Cipriano et al., respectively (in this comparison, we used the same region as Toribio San Cipriano et al. 2016).

We exploit the simultaneous coverage of the $H\alpha$ and [N II] lines to derive oxygen abundances via the strong-line method. As opposed to the direct (T_e -based) method, the strong-line method relies on empirically derived calibrations that can be used to derive abundances from emission-line ratios. Given that the two emission lines used for the N2 strong-line ratio are close in wavelength (and therefore depend less on the reddening correction) and the ratio does not include high-ionization potential lines (e.g., [O III], hence not introducing nontrivial dependencies on the degree of ionization), here we use the N2 line ratio,

$$N2 = \log\left(\frac{[\text{N II}] \lambda 6584}{H\alpha}\right), \quad (2)$$

and adopt the empirical calibration for this line ratio given by Marino et al. (2013). We find oxygen abundances in the range $8.32 < 12 + \log(\text{O}/\text{H}) < 8.40$, with the derived value for 118A being in excellent agreement with the (T_e -derived) value of 8.38 ± 0.06 reported in Toribio San Cipriano et al. (2016) ($12 + \log(\text{O}/\text{H}) = 8.36 \pm 0.08$ vs. 8.38 ± 0.06 for R23 in this work and Toribio San Cipriano et al., respectively).

To derive H II region expansion velocities, we perform Gaussian fits (see Table 7) to a total of six nebular emission lines in the wavelength interval $6500 \text{ \AA} < \lambda < 6800 \text{ \AA}$, which covers the $H\alpha$ line, as well as [N II] $\lambda\lambda 6548, 84$, [S II] $\lambda\lambda 6717, 31$, and He I $\lambda 6678$. The selection of these lines to derive ionized gas kinematics is motivated by the fact that (a) they are among the brightest nebular emission lines; (b) they lie close in wavelength, therefore reducing possible uncertainties introduced by suboptimal wavelength calibrations; and (c) with similar ionization energies, one can assume that these are originating from the same line-emitting gas (McLeod et al. 2015). From the difference between the mean systemic velocities of the two regions of ~ 102 and ~ 105 km s $^{-1}$ (for 118B and 119C, respectively, derived from VLA HI data; Faesi et al. 2014) and the wavelength shifts obtained from the

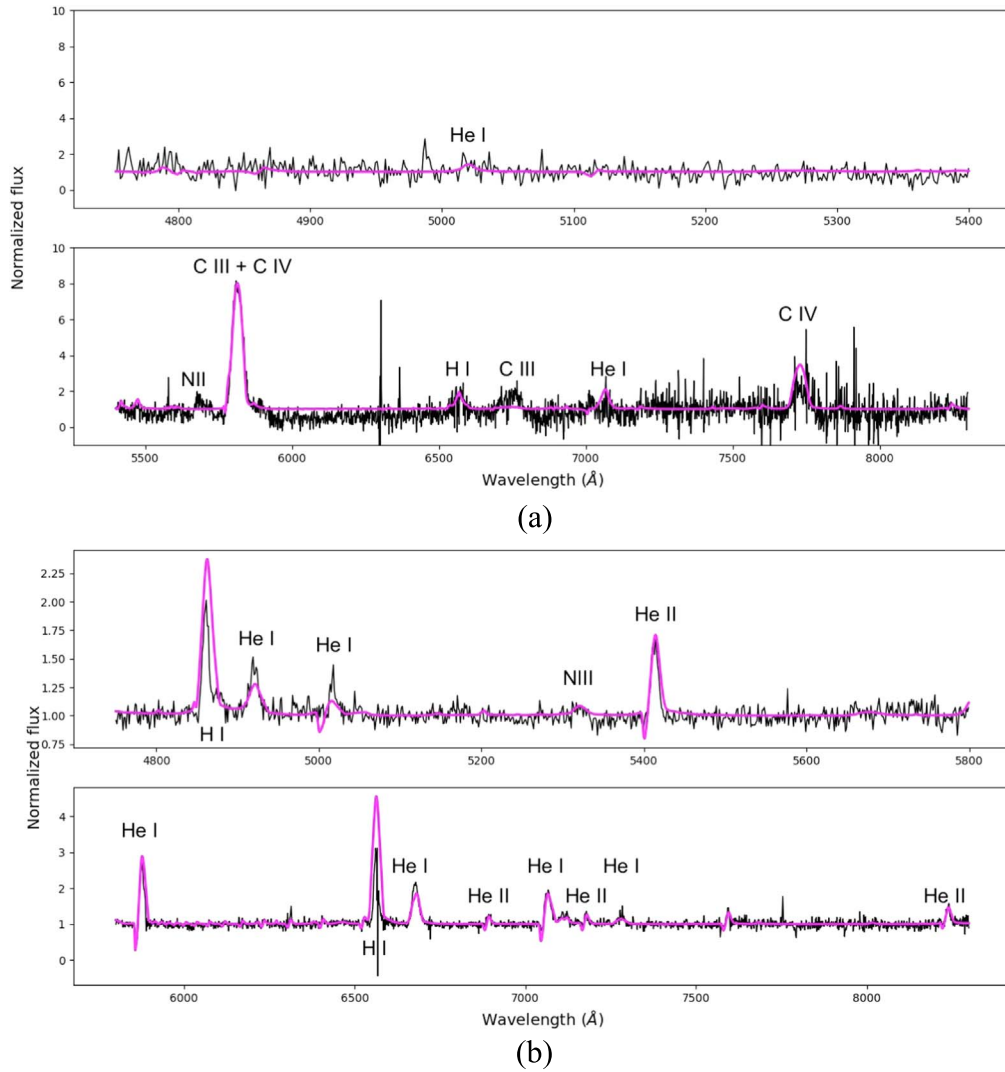


Figure 10. Spectra (black) of the WR stars (a) 118-WR2 and (b) 119-WR1, and the best-fit PoWR model atmospheres (magenta). See Section 3 and Table 4 for details. Prominent lines are labeled.

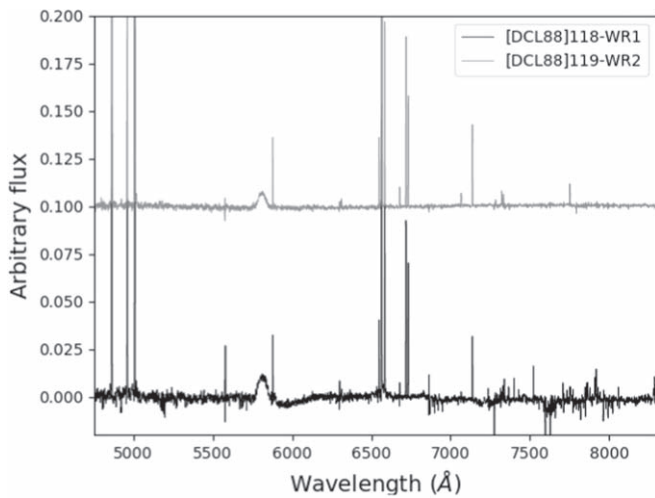


Figure 11. Spectra of the WC stars 118-WR1 (bottom black) and 119-WR2 (top gray). See Section 3 and Table 4 for details.

fitted line centroids, we find expansion velocities of the order of a few times the isothermal sound speed. This is in agreement

with the expansion velocities measured independently by Kruijssen et al. (2019), who obtain a typical H II region expansion velocity of $9.4^{+0.8}_{-0.7}$ km s⁻¹ by dividing the inferred GMC radii (taken to be the Gaussian dispersion of $14.8^{+1.0}_{-0.9}$ pc) by the time it takes stellar feedback to disperse the parent GMC (1.5 ± 0.2 Myr).

4.2. Luminosities, Gas Masses, and Feedback Quantities

As in MC19, we derive H II region luminosities, $L_{\text{H}\alpha}$, from the (extinction-corrected) H α line intensity, and (under the assumption of case B recombination) we convert these to Lyman continuum fluxes, $Q_{\text{H}\alpha} = 7.31 \times L_{\text{H}\alpha} \text{ s}^{-1}$ (Osterbrock & Ferland 2006). We also compute the total ionizing flux, $Q_{0,*}$, for each region as derived from the massive stars within them (all values are reported in Table 6). For this we assume that the stars within R_{90} are spatially coincident and part of the respective regions, i.e., 118A contains 118-1, 118-3, and 118WR-1; 118B contains the star 118-4; 119A encompasses 119-2, 3, 4, 5, 6, 8, and 9; 119-7 and 119WR-1 are in the region 119B; and 119C is being inflated by 119WR-2.

When compared to the photon flux $Q_{0,*}$ derived from the identification of the massive stars, we find that for the case

Table 5
Physical Parameters of the Five H II Regions

Region	R_{90} (pc)	A_V mag	n_e (cm^{-3})	T_e (10^3 K)	$12+\log(\text{O}/\text{H})$	v_{exp} (km s^{-1})	M_{ion} (M_{\odot})
118A	32.5	0.65	62.3 ± 8.3	9.7 ± 0.3	8.32 ± 0.01	17.3 ± 1.0	5.4×10^3
118B	25.7	0.71	41.4 ± 12.7	11.2 ± 0.9	8.39 ± 0.01	27.6 ± 2.6	1.0×10^3
119A	42.2	0.41	84.4 ± 2.8	9.2 ± 0.1	8.36 ± 0.01	12.7 ± 2.1	7.0×10^3
119B	27.6	0.37	55.9 ± 3.1	8.9 ± 0.1	8.40 ± 0.01	8.4 ± 3.8	2.3×10^3
119C	28.6	0.48	75.9 ± 9.0	9.5 ± 0.3	8.38 ± 0.01	11.3 ± 7.1	0.9×10^3

Table 6
Integrated H II Region Properties

Region	$\log Q_{0,*}$ (s^{-1})	$\log L_{0,*}$ (erg s^{-1})	$\log Q_{\text{H}\alpha}$ (s^{-1})	$\log L_{\text{H}\alpha}$ (erg s^{-1})	SFR ($10^{-4} M_{\odot} \text{ yr}^{-1}$)	Σ_{SFR} ($M_{\odot} \text{ yr}^{-1} \text{ pc}^{-2}$)	P_{dir}	P_{ion}	P_w	η_{ion}
118A	49.52	5.7	49.90	38.04	5.8	8.7×10^{-8}	0.015	1.67	1.92	5.0
118B	49.15	5.9	49.01	37.14	0.8	1.9×10^{-8}	0.038	1.28	3.15	15.0
119A	49.66	6.0	50.15	38.28	10.4	9.3×10^{-8}	0.018	2.15	1.38	2.1
119B	49.11	5.3	49.49	37.62	2.3	4.8×10^{-8}	0.0084	1.37	0.40	3.2
119C	49.50	5.6	49.19	37.33	1.1	2.1×10^{-8}	0.016	1.98	0.98	3.0

Note. Column (2): total ionizing photon flux emitted by the massive stars within each region. Column (3): integrated H α luminosity. Column (4): photon flux as derived from $L_{\text{H}\alpha}$. Columns (5) and (6): star formation rate and star formation rate density, respectively. Columns (7), (8), and (9): feedback-related pressure terms P_{dir} , P_{ion} , and P_w (in units of $10^{-10} \text{ dyn cm}^{-2}$), respectively. Column (10): ionized gas mass loading factor. See Appendix A.2 for uncertainties on the obtained quantities.

B–derived photon flux $Q_{\text{H}\alpha}$, only 118B and 119C are consistent with the trend found in the LMC (see Figure 12), i.e., not all of the ionizing photons emitted by the massive stars in these two regions go into producing the observed H α luminosity, and hence $Q_{\text{H}\alpha} < Q_{0,*}$. For the remaining three H II regions, however, the opposite is true, i.e., the derived photon flux cannot account for the observed H α luminosity ($Q_{\text{H}\alpha} > Q_{0,*}$). Our completeness in terms of the massive (O-type) stellar population is most likely significantly better in the analyzed LMC H II regions. Both 118B and 119C contain a single identified massive star (118-4 and 119WR-2, respectively), and the opposite trend observed for 118A, 119A, and 119B might be indicating that we are missing some fraction of massive stars in these three regions. There are several possible reasons for this, which we briefly discuss.

First, we note that there are a few candidate massive stars that could not be reliably classified as O-type stars owing to infilling of the He II line. Second, even with the high spatial resolution *HST* catalog as a reference, crowding remains challenging (particularly in regions 118A and 119A), and higher spatial resolution IFU follow-up observations would be required. The MUSE data discussed here were taken prior to MUSE having AO compatibility in the wide-field mode, which is now available. For example, targeted MUSE+AO observations in the narrow-field mode would allow an order of magnitude better angular resolution, with the capability of reaching ~ 0.3 pc resolution, which is roughly the resolution we achieved for LMC H II regions and a factor of ~ 3 closer to the spatial resolution of *HST*/ACS. Third, some of these stars are likely to be unresolved binaries (e.g., Sana et al. 2012), and as a consequence we are underestimating the emitted photon flux. Lastly, there is likely a population of embedded O stars, which are therefore missed.

We crudely investigate the (in)completeness of our identification algorithm by injecting O stars into a simulated MUSE cube, as described in Appendix A.1. With this procedure we find that we are systematically missing $\approx 30\%$ of the O star population, where the unidentified stars are those with low He II absorption line amplitudes, rather than those in crowded environments. In terms of our observations, this translates into stars not being identified because they are either embedded or faint, low-mass stars. This also shows the unique capability of the combination of high spatial resolution *HST* photometry and MUSE spectroscopy in identifying stars in crowded fields at 2 Mpc.

The combination of unresolved binaries and fainter or embedded stars being missed results in the derived photon fluxes $Q_{0,*}$ being strict lower limits, in particular for three out of the five regions (118A, 119A, 119B). However, assuming that the two single sources in 118B and 119C are the main feedback-driving sources given the lack of other bright stars within them in both the *HST* and the MUSE data (hence assuming a complete census of massive stars within these specific regions), and assuming that the deviation from case B recombination conversion between H α luminosity and ionizing photon flux is due to photon leakage, we can compute the photon escape fraction, $f_{\text{esc}} = (Q_{0,*} - Q_{\text{H}\alpha})/Q_{0,*}$, yielding $\sim 0.28 \pm 0.06$ and $\sim 0.51 \pm 0.10$ for 118B and 119C, respectively. These values are consistent with analytical predictions for the later stages of H II region expansion (Rahner et al. 2017) and recent measurements of the diffuse ionized gas fraction in nearby galaxies (ranging from 0.25 to 0.75; see, e.g., Kreckel et al. 2018; Chevance et al. 2019; Hygate et al. 2019b; Kruijssen et al. 2019). As discussed in Niederhofer et al. (2016), escaping photons are not absorbed in the H II region matter, but will instead contribute to the overall energetics of the host galaxy, consistent with the close correspondence

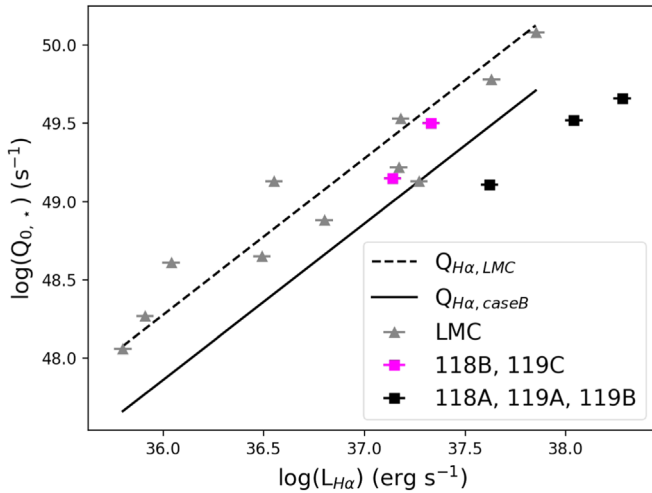


Figure 12. Comparison between the photon flux $Q_{0,*}$ derived from the identification of the massive stars and as derived from case B recombination (solid black line). Gray data points are H II regions in the LMC from MC19, and the dashed line is a fit to the LMC values. Magenta squares are the two regions 118B and 119C; black squares are the remaining three (see Section 4.2).

between the escape fractions estimated for individual H II regions here and the global diffuse ionized gas fractions from the literature quoted above.

To analyze and quantify the feedback effect from massive stars, we proceed in computing feedback-related pressure terms, i.e., the direct radiation pressure, P_{dir} , the pressure of the warm, ionized gas, P_{ion} , and the pressure due to stellar winds, P_w , and they are listed in Table 6.

The direct radiation pressure is evaluated from the combined (bolometric) luminosity L_* of the massive stellar population in each region,

$$P_{\text{dir}} = \frac{3L_*}{4\pi R^2 c}. \quad (3)$$

This is different from the expression used in MC19, which estimates the radiation force density at the rim of a shell rather than the volume-averaged radiation pressure. The pressure of the ionized gas is evaluated from the electron density as

$$P_{\text{ion}} = (n_e + n_H + n_{\text{He}})kT_e \approx 2n_e kT_e, \quad (4)$$

where we assume an H II region temperature of 10^4 K, as well as singly ionized helium. The pressure from stellar winds follows from

$$P_w \simeq 2.3 \times 10^{-12} \left(\frac{L_w}{10^{36} \text{ erg s}^{-1}} \right)^{2/5} \left(\frac{n_0}{0.25 \text{ cm}^{-3}} \right)^{3/5} \times \left(\frac{10^6 \text{ yr}}{t} \right)^{4/5} \text{ dyn cm}^{-2}, \quad (5)$$

with L_w the wind luminosity, $R = R_{90}$, $n_0 = n_e/0.7$ (McLeod et al. 2016), and t the dynamical timescale (MC19).

As already found for H II regions in the LMC and SMC (Lopez et al. 2014; McLeod et al. 2019), the direct radiation pressure is about one to two orders of magnitude lower than the other two pressure terms. Hence, at these evolved H II region stages, the direct radiation pressure contributes to, but never dominates, the expansion of the regions, which is driven by the combination of stellar winds and the pressure of the ionized

gas. This matches the conclusion reached by Kruijssen et al. (2019), who used an independent methodology complementary to ours to investigate the dominant feedback mechanisms driving GMC dispersal across a large fraction of the optical disk of NGC 300.

In terms of P_{dir} , we note that the derived values do not account for photon leakage and likely do not represent a fully sampled massive end of the stellar population (see above). This is particularly true for regions 118A, 119A, and 119B. However, even by assuming that the ionizing photons emitted by a *complete* stellar population are producing the observed $H\alpha$ luminosity and accounting for escaping photons, and hence using $Q_{H\alpha}$ instead of $Q_{0,*}$, P_{dir} would still be one to two orders of magnitude lower than the other two pressure terms.

Furthermore, we compute the mass of the ionized gas according to Osterbrock & Ferland (2006),

$$M_{\text{ion}} \approx Q_{L(H\alpha)} m_p / (n_e \alpha_B), \quad (6)$$

with the proton mass m_p and the case B coefficient α_B , and assuming negligible dust absorption. The inferred ionized gas masses (listed in Table 5) will be used in the following section to derive ionized gas mass loading factors.

4.3. SFRs, Ionized Gas Mass Loading Factors, and Feedback Efficiency

From $L_{H\alpha}$ we derive SFRs according to Kennicutt & Evans (2012),

$$\log(\text{SFR}) (M_\odot \text{ yr}^{-1}) = \log L_{H\alpha} - \log C_{H\alpha} \quad (7)$$

(with $\log C_{H\alpha} = 41.27$; Hao et al. 2011) and, together with R_{90} , the SFR surface density, Σ_{SFR} . We note that using the above $L_{H\alpha}$ –SFR conversion on spatially resolved regions such as the ones studied here introduces a series of caveats, as (i) this conversion is based on an ensemble average over H II regions of different ages, (ii) it was derived for solar abundances, and (iii) it relies on population synthesis models. Indeed, at SFRs below ~ 0.001 – $0.01 M_\odot \text{ yr}^{-1}$, stellar populations in the regions do not fully sample the stellar initial mass function (IMF), leading to the luminosity of the used tracer fluctuating on small spatial scales for a given SFR (Kennicutt & Evans 2012). Tracers of the ionized gas, e.g., the $H\alpha$ luminosity used here, are particularly affected by this, given that these mostly trace the upper end of the IMF. However, under the assumption of the gas and stars in the analyzed regions being physically associated (i.e., the regions being young), deriving SFRs remains a meaningful exercise not only to estimate the level of star formation activity in the youngest regions across NGC 300 and compare these values to those derived for the LMC H II regions but also to evaluate the reliability of using common galaxy-scale analysis methods and relations for cloud-scale studies.

Due to the overall larger sizes and higher luminosities compared to the LMC H II region complexes N44 and N180 (MC19), we find overall higher SFRs in these NGC 300 H II regions. Despite these relatively high SFRs, none of these compare to, e.g., 30 Doradus, one of the most massive star-forming regions in the nearby universe, where SFRs of the order of some $0.02 M_\odot \text{ yr}^{-1}$ over radii of ~ 140 pc have been measured (Ochsendorf et al. 2017).

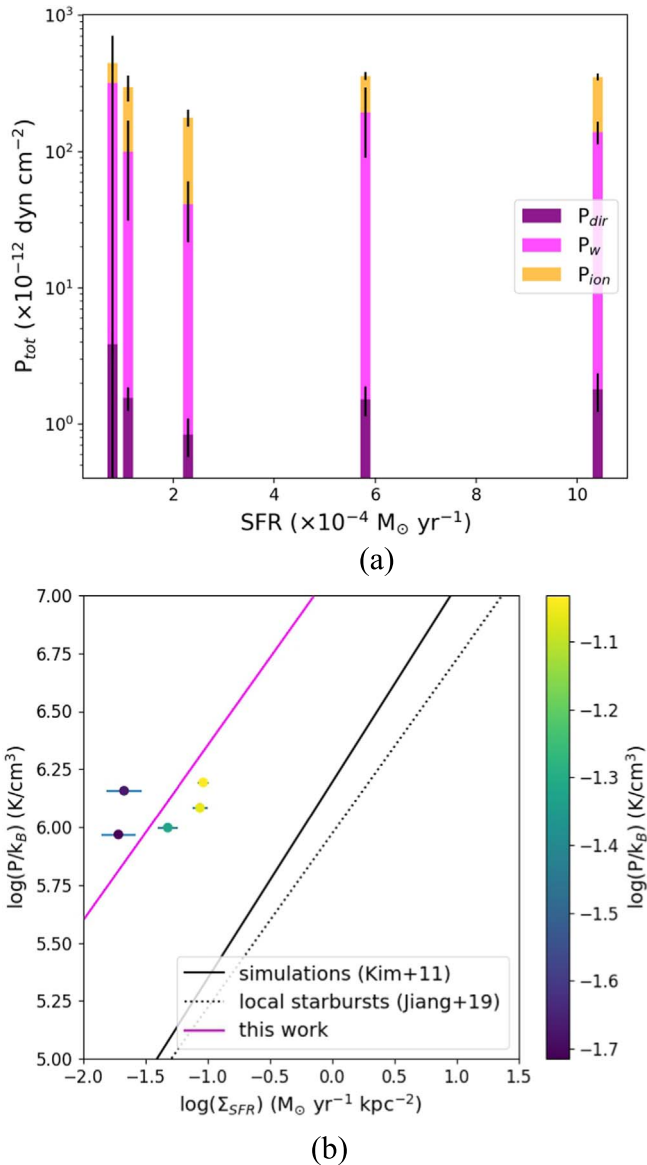


Figure 13. (a) Relative contribution of the various pressure terms to the total pressure as a function of the SFR. (b) Relation between the SFR surface density and the ionized gas pressure. To compare our findings with simulations (Kim et al. 2011) and observations (Jiang et al. 2019) of local analogs of high-redshift galaxies (dashed and dotted lines, respectively), here P_{ion} is in units of K cm^{-3} and Σ_{SFR} in units of $M_{\odot} \text{ yr}^{-1} \text{ kpc}^{-2}$. The solid line shows the simulated relation shifted down by a factor of 30.

Figure 13(a) shows the relative contribution of the various pressure terms to the total pressure as a function of SFR. As found for the LMC regions, the pressure of the ionized gas and the pressure from stellar winds contribute almost equally to the total pressure. An exception to this is 118B, for which we derive the (overall) lowest SFR and highest ionized gas mass loading factor (see below), together with the highest stellar wind pressure term. With 118B being the smallest of the five regions, it also has the highest measured expansion velocity. This region is associated with a single O-type star, the high-mass object [DCL88]118-4, and the measured $\text{H}\alpha$ luminosity of this “single-star” bubble is consistent with the low SFR and strong stellar wind.

Overall, we find a weak trend between the ionized gas pressure and Σ_{SFR} ; however, we refrain from drawing any

conclusions for the NGC 300 H II regions owing to the small number of data points. In this sense, the linear fit in Figure 13(b) is only indicative and associated with a large uncertainty on the slope of the fitted line, and it needs to be revised with the analysis of the full MUSE data set across NGC 300. This trend is observed throughout cosmic time from, e.g., $z = 2.5$ $\text{H}\alpha$ emitters (Shimakawa et al. 2015) to local analogs of these (Jiang et al. 2019), as well as in simulations (Kim et al. 2011). Figure 13(b) shows our sample of five H II regions together with the relations derived for nearby compact starbursts (Jiang et al. 2019) and simulations (Kim et al. 2011). It is widely accepted that on the scales of small, individual star-forming regions, other galaxy-wide scaling relations (e.g., the Kennicutt–Schmidt relation) are no longer valid, and, as discussed in Kruijssen & Longmore (2014) (see also Section 5), the main reason for these galaxy-wide scaling relations breaking down on small scales is that these trace time-dependent phenomena such as the conversion of gas into stars, of which single regions are mere snapshots. One would therefore conclude that trying to look for such relations for individual regions is not particularly insightful.

However, there are cases in which properties derived by integrating over entire galaxies can be overestimated. This is the case of the $P_{\text{ion}}-\Sigma_{\text{SFR}}$ relation: as discussed in Kewley et al. (2019), electron densities and gas pressures derived from integrated galaxy spectra are contaminated by the diffuse ionized gas (DIG; caused by H II region photon leakage, shock excitation, and dust-reprocessed radiation). This can result in overestimates of these quantities, which makes a small-scale (< 100 pc) investigation of the $P_{\text{ion}}-\Sigma_{\text{SFR}}$ relation meaningful and necessary. Indeed, the location of the NGC 300 H II regions in the parameter space shown in Figure 13(b) is consistent with the above argument.

We combine the mass and kinematics of the ionized gas with the SFR to derive the ionized gas mass loading factors (i.e., the mass outflow rate of the ionized gas due to stellar feedback per unit SFR) for the five H II regions,

$$\eta_{\text{ion}} = \frac{\dot{M}_{\text{ion}}}{\text{SFR}}, \quad (8)$$

where $\dot{M}_{\text{ion}} = M_{\text{ion}}v/R_{90}$ is the ionized gas mass outflow rate. Stellar feedback in these regions is dominated by stellar winds and the ionized gas pressure, which therefore are driving the mass removal quantified by η_{ion} . For all five regions we find $\eta_{\text{ion}} > 1$, implying a negative feedback effect. The combined effect of stellar winds and ionized gas pressure is therefore efficiently quenching star formation by clearing the gas and driving the expansion of the H II regions.

Kruijssen et al. (2019) recently combined 20 pc resolution maps of molecular gas and $\text{H}\alpha$ emission in NGC 300 to derive a cloud-scale total gas mass loading factor of $\eta_{\text{tot}} = 40^{+31}_{-18}$ across the star-forming disk of NGC 300. This mass loading factor exceeds our values by about an order of magnitude, which would suggest that the ionized gas mass does not dominate the mass budget of the expanding bubbles. Indeed, both D118 and D119 are associated with nearly $10^5 M_{\odot}$ of molecular gas (Kruijssen et al. 2019), which is roughly an order of magnitude larger than our ionized gas masses. Therefore, the difference in mass loading factors either may be a direct result of the multiphase nature of the feedback-driven bubbles or may imply that these two H II region complexes are particularly young and still contain a large molecular gas reservoir.

The range of values for η_{ion} derived for the five NGC 300 H II regions are larger than those found for star-forming clumps in low- z luminous star-forming galaxies (Arribas et al. 2014), where η_{ion} is generally below unity and no negative feedback is observed. We note that while they are not entire galaxies, the regions analyzed in Arribas et al. (2014) have kiloparsec-scale sizes. These apertures are therefore likely to contain populations of unresolved H II regions, as well as DIG, the latter also contributing to the measured H α luminosity and therefore to the derived SFRs, resulting in lower ionized gas mass loading factors. Galaxy-wide IFU studies that resolve individual H II regions will therefore deliver groundbreaking progress thanks to the ability to efficiently remove large-scale contaminating factors to galaxy scaling relations.

5. Outlook

The data cubes used in this work are a mere 2 of a 35-pointing mosaic that covers most of the star-forming disk of NGC 300. The full MUSE NGC 300 data set samples >100 individual H II regions, as well as a large number of planetary nebulae, supernova remnants, red supergiants, and X-ray binaries. In McLeod et al. (2020, in preparation) we will analyze the full NGC 300 data set in terms of massive stars, stellar feedback, and H II region properties. In this forthcoming publication we will not only deliver all the quantities derived here for the entire H II region population in our data set, hence producing comprehensive catalogs of massive stars, gas kinematics, physical H II region parameters, and feedback quantities; we will also publish the reduced data cubes for the community to use.

Together with the NGC 300 catalogs and data set, we will also publish the analysis methods and techniques used in this paper as PYTHON Notebooks, which will be readily applicable to generic IFU data sets. Below, we briefly discuss some of the more immediate deliverables of the full MUSE NGC 300 data.

5.1. Finding Wolf-Rayet Stars

In terms of stellar feedback analyses, WR stars are among the dominant feedback sources owing to their strong ionizing spectra, powerful stellar winds, and the fact that most of these are supernova progenitors. In this context, the decrease in strength of stellar winds at lower metallicities is particularly interesting. As opposed to the inner regions of the Magellanic Clouds, which have a rather shallow metallicity gradient (Feast et al. 2010; Choudhury et al. 2018), the star-forming disk of NGC 300 has a steeper gradient (e.g., Toribio San Cipriano et al. 2016), and we would therefore expect weaker WR star winds in the outer part of the disk. Moreover, because the ratio of WC to WN stars is shown to be sensitive to metallicity (Massey 1996), we would also expect to find more WN stars in the outer parts of NGC 300. Hence, identifying WR stars is essential when studying the feedback energy budget of H II regions throughout galaxies.

The WR content of NGC 300 has been subject to several past studies (e.g., Breysacher et al. 1997; Schild et al. 2003), and the number of known WR stars in the galaxy is currently at ~ 60 sources. These studies are predominantly based on narrowband imaging, combined with spectroscopic follow-up for selected sources. Because MUSE covers the entire optical regime (i.e., 4750–9350 Å) and we are able to make images of any narrow- or broadband filter within the instrument’s

wavelength coverage, we are able to simultaneously photo-metrically identify and spectroscopically confirm WC, WO, and WN stars with the same data set. In McLeod et al. (2019, in preparation) we will apply this to the entire $7' \times 5'$ MUSE mosaic of NGC 300. Because we are also able to retrieve independent metallicity measurements from the H II regions, the planetary nebulae, and the red supergiants in the mosaic, we will be able to directly analyze the contribution of WR winds and radiation to the feedback energy budget of the individual H II regions as a function of metallicity.

5.2. Connecting Feedback to Integrated H II Region Properties across the NGC 300 Disk

In the context of the dependence of stellar feedback on the properties of the regions the massive stars form in, i.e., gas-phase metallicities, gas densities, star formation history (e.g., Gogarten et al. 2010), and location within the galaxy, it is imperative to obtain H II region properties and massive stellar censuses for a statistically significant sample, rather than only for a handful of well-studied regions.

As already introduced in the previous section, large IFU surveys of entire galaxies allow, for example, metal abundance determinations from hundreds of objects representing different evolutionary stages or epochs of star formation *simultaneously*, e.g., H II regions (e.g., Toribio San Cipriano et al. 2016), planetary nebulae (e.g., Stasińska et al. 2013), and red supergiants (e.g., Gazak et al. 2015). By connecting WC/WN populations to gas-phase metal abundances (e.g., C/O, N/O), this will enable us to directly relate feedback to the chemical enrichment and dispersal history.

Of particular interest will be the ability to compare the derived properties of hundreds of H II regions to feedback models, e.g., WARPFIELD (Rahner et al. 2019). Specifically, because the observations sample the timeline of star formation, such comparisons will enable the analysis of time-dependent H II region diagnostics. A first comparison between these and SITELLE IFU observations of NGC 628 (Rousseau-Nepton et al. 2018) is shown in Pellegrini et al. (2019), which demonstrates the power to harness the observations to test the models, and to harness the models to understand the observations.

5.3. The Multiphase Interstellar Medium and the Small-scale Physics of Star Formation and Feedback

As discussed in Kruijssen & Longmore (2014), scaling relations like the Kennicutt–Schmidt relation break down on the small scales of individual GMCs and H II regions. Galactic scaling relations are built from integrated observations of regions that are large enough to fully sample the complete evolutionary timeline from cloud formation to star formation and feedback-driven dispersal—the small-scale breakdown is due to individual regions representing single evolutionary snapshots of this timeline rather than an ensemble average.

Kruijssen et al. (2018) developed a statistical method for translating this statistical behavior of the relation between molecular gas (e.g., traced by CO) and star formation (e.g., traced by H α) to empirical constraints on baryon cycle in the ISM down to GMC scales. This methodology provides direct measurements of the molecular cloud lifetime, the feedback timescale (i.e., the time for which GMCs and H II regions coexist), the feedback dispersal velocity, the cloud-scale total

mass loading factor, and the integrated star formation efficiency per star formation event. This method has previously been applied to NGC 300 using CO and narrowband H α data (Kruijssen et al. 2019; see also the comparisons to our results throughout Section 4), as well as about a dozen other nearby galaxies (Chevance et al. 2019; Hygate et al. 2019b).

While the MUSE coverage across a sizable part of NGC 300's star-forming disk is ideally suited for further applications of this methodology, of particular interest is the fact that any tracer probing part of the evolutionary timeline of GMCs and H II regions can be used to construct a multitracers timeline of star formation and stellar feedback. Ward et al. (2019) provide a recent example, measuring the H I cloud lifetime in the LMC. With the MUSE data obtained here, we will be able to measure the emission lifetimes of a wide variety of ionized emission lines, in conjunction with the physical quantities derived already by combining CO and H α emission.

5.4. The Diffuse Ionized Gas

As discussed in Kewley et al. (2019) and in Section 4.3, small-scale (<100 pc) observations are the missing piece to disentangle the contribution of contaminating factors to galaxy-wide quantities and relations between these. A prominent example of this is the effect of the diffuse ionized gas on measurements of, e.g., abundance gradients, ionized gas pressures, or SFRs, which can be grossly overestimated. Moreover, the diffuse ionized gas contamination is scale dependent, and spatially resolved observations of individual H II regions across entire galaxies are therefore vital in better constraining the quantities that are used to derive common galaxy-wide relations. The wide-field coverage of the full MUSE mosaic is ideally suited for combining statistical methods to isolate the diffuse ionized gas (e.g., Hygate et al. 2019a) with a spatially resolved, region-by-region census of individual H II regions. We plan to explore this possibility in future work.

6. Summary and Conclusions

This article presents a pilot study of resolved stellar feedback in five H II regions in the nearby spiral galaxy NGC 300, covered with a $1' \times 2'$ IFU data set from the MUSE instrument. We demonstrate that at 2 Mpc distance, in combination with high spatial resolution *HST* photometry, IFU data can be used to simultaneously identify the feedback-driving massive stars and obtain kinematics, physical properties, and feedback-related quantities of the individual star-forming regions hosting the massive stars.

We spectroscopically identify 13 previously unknown O-type stars associated with the H II regions and derive atmospheric parameters. Moreover, we revisit the spectral type of two WR stars and confirm the WR nature of a further two previously known candidates. The novelty of combining high angular resolution *HST* data with the ground-based IFU cubes demonstrates that at a distance of 2 Mpc we are able to deblend individual sources in crowded star-forming regions.

By comparing the ionizing photon budget of each region as derived from its stellar content to that derived from the measured H α luminosity, we conclude that the massive star census is likely not fully complete for three of the five H II regions (118A, 119A, and 119B). The incompleteness is likely due to a combination of unresolved binaries and embedded or

faint O-type stars, and the derived combined photon fluxes $Q_{0,*}$ of these regions are therefore strict lower limits. For two of the five H II regions we can assume a complete census of massive, feedback-driving stars, and for these we find that the derived fraction of photons escaping from the H II regions is 28% and 51%, consistent with the later stages of H II region expansion. If measured for a large number of H II regions across an entire galaxy, the escape fraction can be compared to the diffuse H α emission of the NGC 300 disk to evaluate the number of photons leaking from the H II region and therefore going into the heating budget of the galaxy. Kruijssen et al. (2019) perform this measurement for the entire star-forming disk of NGC 300 and find a diffuse ionized gas fraction of 33%, within the range spanned by the two H II regions for which we can currently calculate this number. Targeted follow-up IFU observations with higher angular resolution (e.g., AO-assisted MUSE narrow-field mode observations) and combined with near-IR spectroscopy will allow us to obtain a more complete census of massive stars.

For the H II regions discussed here we derive ionized gas kinematics and compute feedback-related pressure terms, luminosities, SFRs and SFR surface densities, ionized gas masses, ionized gas mass loading factors, oxygen abundances, electron densities, and temperatures. By comparing the obtained quantities to a similar study of H II regions in the LMC, we confirm that the dynamics of the H II regions is dominated by the warm ionized gas and stellar winds, while the direct radiation pressure is ~ 2 orders of magnitude lower than the former two. Moreover, we compare the ionized gas mass loading factors derived for the five H II regions to the *total* gas mass loading factor derived for the NGC 300 disk (Kruijssen et al. 2019) and find that the mass budget of the expanding bubbles is not dominated by the ionized gas. This is either directly linked to the multiphase nature of these regions or indicating very early evolutionary stages and consequently higher molecular gas masses.

We furthermore take advantage of being able to derive the pressure of the ionized gas, enabling us to evaluate the $P_{\text{ion}}-\Sigma_{\text{SFR}}$ relation without the contamination by the diffuse ionized gas, which is problematic at large (kiloparsec) scales, where P_{ion} values are systematically overestimated. Carried out over the full MUSE mosaic of NGC 300, this will, for the first time, allow us to confidently derive this relation (as well as other scaling relations) without the diffuse ionized gas contamination.

In terms of a broader picture of the role of stellar feedback in star-forming galaxies, we briefly discuss the implications and potential outcomes of applying the analysis techniques and methods derived in this proof-of-concept study on large IFU data sets covering entire galaxies. A first study of this scale will be presented in a forthcoming publication encompassing the central $7' \times 5'$ region covering most of the star-forming disk of NGC 300. This short study therefore explores the necessary techniques for resolved stellar feedback studies in nearby galaxy scales. These will be readily applicable to data sets from ongoing and forthcoming nearby galaxy IFU surveys and therefore deliver the needed statistics to observationally quantify stellar feedback over representative galactic properties and environments.

Support for this work was provided by NASA through the NASA Hubble Fellowship grant HF2-51442.001 awarded by

the Space Telescope Science Institute, which is operated by the Association of Universities for Research in Astronomy, Inc., for NASA, under contract NAS5-26555. This research is partly supported by a Marsden grant from the Royal Society of New Zealand (A.F.M.). It is based on observations made with ESO Telescopes at the Paranal Observatory under program ID 098. B-0193. J.M.D.K. and M.C. gratefully acknowledge funding from the German Research Foundation (DFG) in the form of an Emmy Noether Research Group (grant No. KR4801/1-1) and the DFG Sachbeihilfe (grant No. KR4801/2-1). J.M.D.K. gratefully acknowledges funding from the European Research Council (ERC) under the European Union’s Horizon 2020 research and innovation program via the ERC Starting Grant MUSTANG (grant agreement No. 714907) and Sonderforschungsbereich SFB 881 “The Milky Way System” (subproject B2) of the DFG. A.F.M. thanks M. Krumholz and C. McKee for the useful discussion and S. Kamann for the invaluable help with PampelMuse. P.Z. acknowledges support by the Forschungsstipendium (ZE 1159/1-1) of the German Research Foundation, particularly via the project 398719443. C.M.F. acknowledges support from the National Science Foundation under award No. 1903946.

Facilities: HST(ACS), VLT(MUSE).

Software: MUSE pipeline (Weilbacher et al. 2015), PampelMuse (Kamann et al. 2013), PySpecKit (Ginsburg & Mirocha 2011), PyNeb (Luridiana et al. 2015), Astropy (Price-Whelan et al. 2018).

Appendix A

A.1. Completeness

As described in Section 4.2, we are most likely not detecting a fraction of the O stars in the clusters owing to crowding, which at a distance of 2 Mpc is challenging even in the *HST* data. We therefore perform completeness tests to estimate the fraction of unidentified O-type stars. For this, we proceed as follows:

1. We simulate a $20'' \times 20''$ *HST* image (i.e., $20'' = 400$ pixels) by populating it with randomly located Gaussian sources.
2. With the simulated *HST* image we produce a data cube spanning from 5350.28 to 5469.03 Å, i.e., covering the He II $\lambda 5411$ absorption line used to identify and classify the O stars, by propagating the simulated image along the spectral axis and adding random Gaussian noise to each frame; the spectral axis of the simulated data cube has the same sampling as the MUSE data (1.25 Å).
3. We produce a sample of synthetic O star spectra, thus having an He II $\lambda 5411$ absorption line; for this we randomly sample line amplitudes and line widths, and we add noise to the spectra.
4. Next, we identify the (simulated) stars in the 97th brightness percentile (motivated by the brightness of the O stars identified in the real data) and assign the pixels associated with these stars a spectrum as created above; all the other stars (because they are not O stars) will not have this absorption line.
5. We then rebin the synthetic *HST* data cube to the resolution of MUSE, i.e., we obtain a synthetic MUSE data cube with 100×100 pixels (with a spatial sampling of 0.2 pixel^{-1} , this exactly corresponds to $20'' \times 20''$); pixels are averaged and combined.
6. After rebinning, we further convolve the synthetic MUSE cube to a resolution of $\approx 1''$, so to the seeing-limited resolution of Field 2 (see Table 1).
7. Finally, we proceed in extracting stellar spectra and identifying O stars as per Section 3 based on the synthetic *HST* star catalog.

The above procedure is bootstrapped 100 times to account for random sampling statistics, and we repeat the above procedure for different stellar densities to assess the completeness of identified O stars. This is shown in Figure 14, which shows the average number of identified stars as a function of stellar density (with $\sim 0.16 \text{ stars arcsec}^{-2}$ being the mean average density

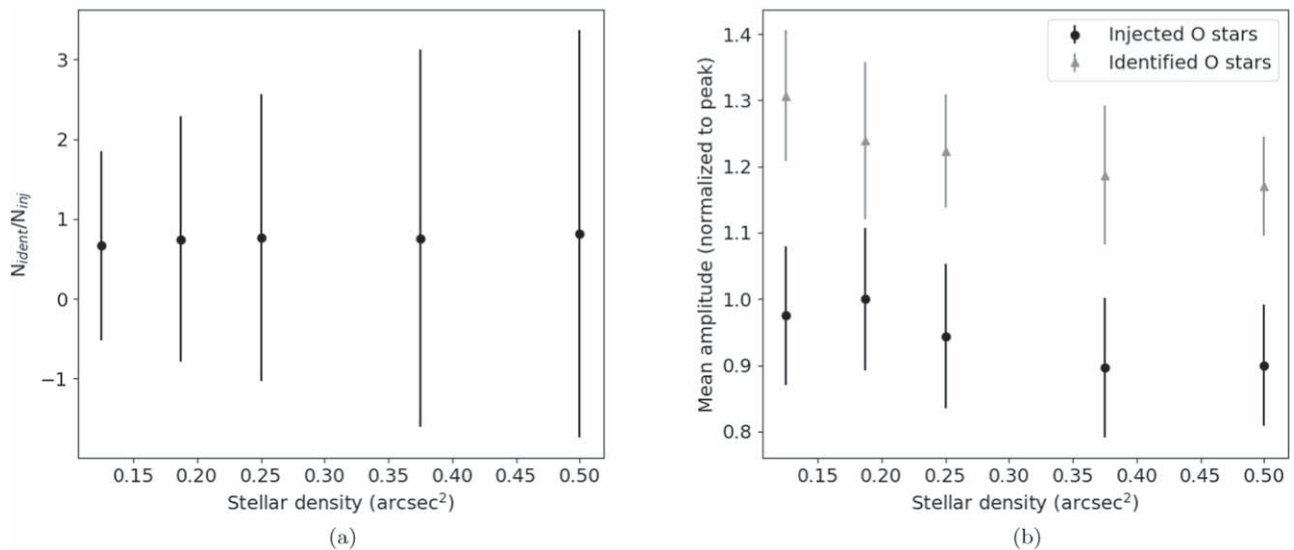


Figure 14. (a) Ratio of the mean number of identified to injected O stars in the simulated MUSE cube as a function of stellar density, as described in Appendix A.1; errors correspond to the standard deviation of the number of identified stars per bootstrap. (b) Mean amplitude of the He II absorption line of the injected and identified O stars, showing that the sample of identified O stars is, on average, more luminous owing to fainter stars being unidentified.

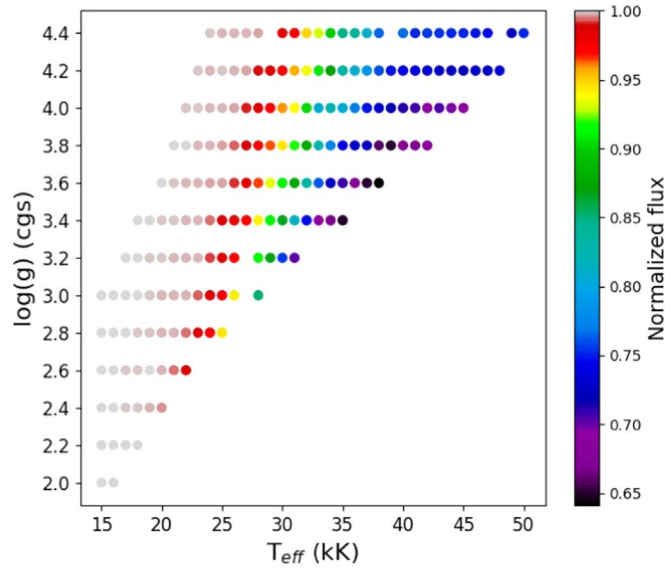


Figure 15. Effective temperature vs. surface gravity from the PoWR model grid (Hainich et al. 2019), color-coded by the depth of the He II $\lambda 5411$ line of each synthetic spectrum.

Table 7
Gaussian Line Centroid Fits (First Row for Each Region) and Centroid Shifts with Respect to the Rest Wavelength (Second Row for Each Region)

Region	[N II] $\lambda 6548$	H α	[N II] $\lambda 6584$	He I $\lambda 6678$	[S II] $\lambda 6717$	[S II] $\lambda 6731$	H β
118A	6550.68 \pm 0.16	6565.37 \pm 0.01	6586.05 \pm 0.05	6680.82 \pm 0.54	6719.17 \pm 0.07	6733.54 \pm 0.09	4863.24 \pm 0.02
	2.58 \pm 0.16	2.60 \pm 0.01	2.55 \pm 0.05	2.62 \pm 0.53	2.73 \pm 0.07	2.72 \pm 0.09	1.91 \pm 0.02
118B	6550.90 \pm 0.36	6565.69 \pm 0.02	6586.29 \pm 0.12	6681.06 \pm 2.09 \pm	6719.35 \pm 0.13	6733.71 \pm 0.18	4863.58 \pm 0.08
	2.80 \pm 0.36	2.92 \pm 0.02	2.79 \pm 0.12	2.86 \pm 2.09	2.91 \pm 0.13	2.89 \pm 0.18	2.25 \pm 0.08
119A	6550.64 \pm 0.09	6565.35 \pm 0.01	6586.01 \pm 0.03	6719.14 \pm 0.04	6733.50 \pm 0.06	6680.81 \pm 0.44	4863.19 \pm 0.02
	2.54 \pm 0.09	2.58 \pm 0.01	2.51 \pm 0.03	2.61 \pm 0.44	2.70 \pm 0.04	2.68 \pm 0.06	1.86 \pm 0.02
119B	6550.55 \pm 0.17	6565.25 \pm 0.01	6585.94 \pm 0.05	6680.66 \pm 0.99	6719.03 \pm 0.08	6733.39 \pm 0.11	4863.11 \pm 0.03
	2.45 \pm 0.17	2.48 \pm 0.01	2.44 \pm 0.05	2.46 \pm 0.99	2.59 \pm 0.08	2.57 \pm 0.11	1.78 \pm 0.03
119C	6550.60 \pm 0.35	6565.37 \pm 0.02	6585.99 \pm 0.11	6680.90 \pm 1.57	6719.08 \pm 0.13	6733.44 \pm 0.18	4863.21 \pm 0.06
	2.50 \pm 0.35	2.60 \pm 0.02	2.49 \pm 0.11	2.70 \pm 1.57	2.63 \pm 0.13	2.62 \pm 0.18	1.90 \pm 0.06

Note. All units are in \AA .

based on the *HST* photometry and the limiting magnitude of the MUSE data), as well as the mean amplitude of the He II absorption line (normalized to peak).

Figure 14 illustrates how at ~ 0.7 the average fraction of identified O stars (i.e., with respect to injected O stars) is roughly constant over the explored stellar density range, and that the main contributing factor to not identifying stars lies in their effective temperature: O stars with lower T_{eff} (i.e., shallower He II absorption lines; see Figure 15) are systematically identified less than brighter, hotter stars.

A.2. Uncertainty Estimation

Values reported in Tables 5 and 6 are derived via Gaussian fitting to the integrated spectra of the five H II regions, i.e., from the circular apertures shown in Figure 5. The uncertainties of the computed quantities are therefore obtained by rigorously propagating the errors from the Gaussian fits to the various

emission lines (see Table 7) through the various steps in computing them, including uncertainties coming from the extinction correction. Given the small uncertainties on the distance to NGC 300 (Dalcanton et al. 2009), we do not include it in our calculations. For brevity we do not report the propagated uncertainties in Tables 5 and 6. An exception to this are the luminosities of the WR stars, the values of which are from the best-fit PoWR grid model, and for which we assume an accommodating 20% uncertainty (see Section 3).

A.3. Determination of R_{90}

To determine R_{90} , we crop the integrated H α map (by eye) to contain only the relevant, individual regions (see Figure 16). These submaps are then used as input for the radial profile algorithm, which determines the radius containing 90% of the H α flux.

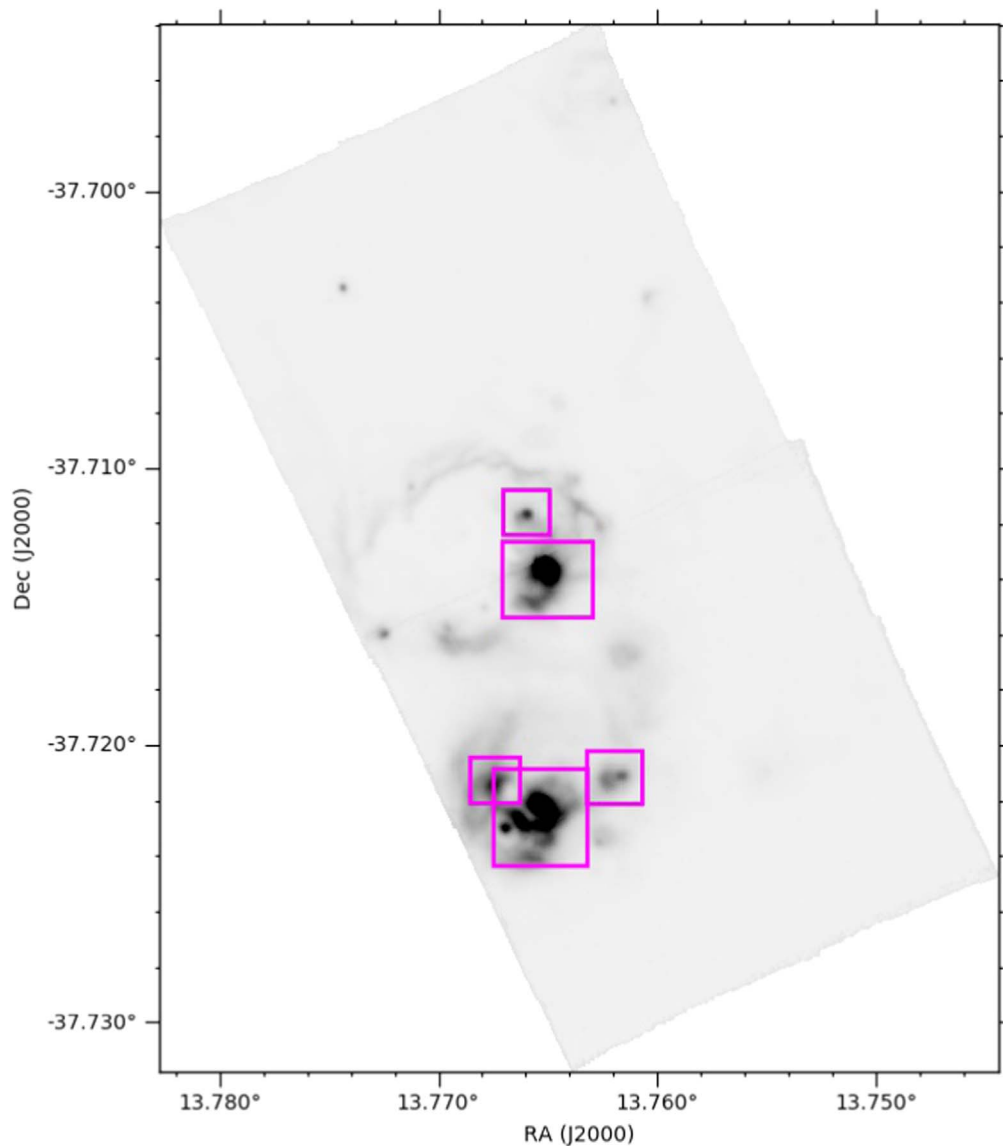


Figure 16. $H\alpha$ map; magenta regions were used to determine R_{90} , defined as the radius (starting from the central coordinates of the respective regions) that encompasses 90% of the $H\alpha$ emission.

ORCID iDs

Anna F. McLeod <https://orcid.org/0000-0002-5456-523X>

Daniel R. Weisz <https://orcid.org/0000-0002-6442-6030>

Peter Zeidler <https://orcid.org/0000-0002-6091-7924>

Julianne J. Dalcanton <https://orcid.org/0000-0002-1264-2006>

Steven N. Longmore <https://orcid.org/0000-0001-6353-0170>

Christopher M. Faesi <https://orcid.org/0000-0001-5310-467X>

Nell Byler <https://orcid.org/0000-0002-7392-3637>

References

- Arribas, S., Colina, L., Bellocchi, E., Maiolino, R., & Villar-Martín, M. 2014, *A&A*, **568**, A14
- Bacon, R., Accardo, M., Adjali, L., et al. 2010, *Proc. SPIE*, **7735**, 773508
- Bate, M. R. 2009, *MNRAS*, **392**, 590
- Bresolin, F., Gieren, W., Kudritzki, R.-P., Pietrzyński, G., & Przybilla, N. 2002, *ApJ*, **567**, 277
- Breysacher, J., Azzopardi, M., Testor, G., & Muratorio, G. 1997, *A&A*, **326**, 976
- Burstein, D., & Heiles, C. 1984, *ApJS*, **54**, 33
- Butler, D. J., Martínez-Delgado, D., & Brandner, W. 2004, *AJ*, **127**, 1472
- Byler, N., Dalcanton, J. J., Conroy, C., et al. 2018, *ApJ*, **863**, 14
- Cardelli, J. A., Clayton, G. C., & Mathis, J. S. 1989, *ApJ*, **345**, 245
- Chevance, M., Kruijssen, J. M. D., Hygate, A. P. S., et al. 2019, *MNRAS*, in press
- Choi, J., Dotter, A., Conroy, C., et al. 2016, *ApJ*, **823**, 102
- Choudhury, S., Subramaniam, A., Cole, A. A., & Sohn, Y. J. 2018, *MNRAS*, **475**, 4279
- Crain, R. A., Schaye, J., Bower, R. G., et al. 2015, *MNRAS*, **450**, 1937
- Crowther, P. A. 2007, *ARA&A*, **45**, 177
- Crowther, P. A., Dessart, L., Hillier, D. J., Abbott, J. B., & Fullerton, A. W. 2002, *A&A*, **392**, 653
- Dalcanton, J. J., Williams, B. F., Seth, A. C., et al. 2009, *ApJS*, **183**, 67
- Dale, J. E., Ngoumou, J., Ercolano, B., & Bonnell, I. A. 2014, *MNRAS*, **442**, 694
- Deharveng, L., Caplan, J., Lequeux, J., et al. 1988, *A&AS*, **73**, 407
- Dotter, A. 2016, *ApJS*, **222**, 8
- Faesi, C. M., Lada, C. J., & Forbrich, J. 2018, *ApJ*, **857**, 19

- Faesi, C. M., Lada, C. J., Forbrich, J., Menten, K. M., & Bouy, H. 2014, *ApJ*, **789**, 81
- Feast, M. W., Abedigamba, O. P., & Whitelock, P. A. 2010, *MNRAS*, **408**, L76
- Gazak, J. Z., Kudritzki, R., Evans, C., et al. 2015, *ApJ*, **805**, 182
- Gies, D. R., & Bolton, C. T. 1986, *ApJS*, **61**, 419
- Ginsburg, A., & Mirocha, J. 2011, PySpecKit: Python Spectroscopic Toolkit, v0.1.22, Astrophysics Source Code Library, ascl:1109.001
- Gogarten, S. M., Dalcanton, J. J., Williams, B. F., et al. 2010, *ApJ*, **712**, 858
- Gray, R. O., & Corbally, C. J. 2009, *Stellar Spectral Classification* (Princeton, NJ: Princeton Univ. Press)
- Hainich, R., Ramachandran, V., Shenar, T., et al. 2019, *A&A*, **621**, A85
- Hao, C.-N., Kennicutt, R. C., Johnson, B. D., et al. 2011, *ApJ*, **741**, 124
- Hopkins, P. F., Narayanan, D., & Murray, N. 2013, *MNRAS*, **432**, 2647
- Hygate, A. P. S., Kruijssen, J. M. D., Chevance, M., et al. 2019a, *MNRAS*, **488**, 2800
- Hygate, A. P. S., Kruijssen, J. M. D., Chevance, M., et al. 2019b, *MNRAS*, submitted
- Jiang, T., Malhotra, S., Yang, H., & Rhoads, J. E. 2019, *ApJ*, **872**, 146
- Kamann, S., Wisotzki, L., & Roth, M. M. 2013, *A&A*, **549**, A71
- Kennicutt, R. C., & Evans, N. J. 2012, *ARA&A*, **50**, 531
- Kerton, C. R., Ballantyne, D. R., & Martin, P. G. 1999, *AJ*, **117**, 2485
- Kewley, L. J., Nicholls, D. C., & Sutherland, R. S. 2019, *ARA&A*, **57**, 511
- Kim, C.-G., Kim, W.-T., & Ostriker, E. C. 2011, *ApJ*, **743**, 25
- Kreckel, K., Faesi, C., Kruijssen, J. M. D., et al. 2018, *ApJL*, **863**, L21
- Kruijssen, J. M. D., & Longmore, S. N. 2014, *MNRAS*, **439**, 3239
- Kruijssen, J. M. D., Schruha, A., Chevance, M., et al. 2019, *Natur*, **569**, 519
- Kruijssen, J. M. D., Schruha, A., Hygate, A. P. S., et al. 2018, *MNRAS*, **479**, 1866
- Krumholz, M. R., Bate, M. R., Arce, H. G., et al. 2014, in *Protostars and Planets VI*, ed. H. Beuther et al. (Tucson, AZ: Univ. Arizona Press), 243
- Lopez, L. A., Krumholz, M. R., Bolatto, A. D., et al. 2014, *ApJ*, **795**, 121
- Luridiana, V., Morisset, C., & Shaw, R. A. 2015, *A&A*, **573**, A42
- Marino, R. A., Rosales-Ortega, F. F., Sánchez, S. F., et al. 2013, *A&A*, **559**, A114
- Massey, P. 1996, in *Liege Int. Astrophysical Coll. 33, Wolf-Rayet stars in the framework of stellar evolution*, ed. J. M. Vreux (Liege: Universite de Liege, Institut d'Astrophysique), 361
- McKee, C. F., van Buren, D., & Lazareff, B. 1984, *ApJL*, **278**, L115
- McLeod, A. F., Dale, J. E., Evans, C. J., et al. 2019, *MNRAS*, **486**, 5263
- McLeod, A. F., Dale, J. E., Ginsburg, A., et al. 2015, *MNRAS*, **450**, 1057
- McLeod, A. F., Gritschneider, M., Dale, J. E., et al. 2016, *MNRAS*, **462**, 3537
- Niederhofer, F., Hilker, M., Bastian, N., & Ercolano, B. 2016, *A&A*, **592**, A47
- Noeske, K. G., Weiner, B. J., Faber, S. M., et al. 2007, *ApJL*, **660**, L43
- Ochsendorf, B. B., Zinnecker, H., Nayak, O., et al. 2017, *NatAs*, **1**, 784
- Osterbrock, D. E., & Ferland, G. J. 2006, *Astrophysics of Gaseous Nebulae and Active Galactic Nuclei* (Sausalito, CA: University Science Books)
- Pellegrini, E. W., Baldwin, J. A., & Ferland, G. J. 2010, *ApJS*, **191**, 160
- Pellegrini, E. W., Rahner, D., Reissl, S., et al. 2019, arXiv:1909.09651
- Price-Whelan, A. M., Sipőcz, B. M., Günther, H. M., et al. 2018, *AJ*, **156**, 123
- Rahner, D., Pellegrini, E. W., Glover, S. C. O., & Klessen, R. S. 2017, *MNRAS*, **470**, 4453
- Rahner, D., Pellegrini, E. W., Glover, S. C. O., & Klessen, R. S. 2019, *MNRAS*, **483**, 2547
- Ramachandran, V., Hainich, R., Hamann, W. R., et al. 2018, *A&A*, **609**, A7
- Ramachandran, V., Hamann, W. R., Oskino, L. M., et al. 2019, *A&A*, **625**, A104
- Richer, H. B., Pritchett, C. J., & Crabtree, D. R. 1985, *ApJ*, **298**, 240
- Rizzi, L., Bresolin, F., Kudritzki, R.-P., Gieren, W., & Pietrzyński, G. 2006, *ApJ*, **638**, 766
- Roth, M. M., Sandin, C., Kamann, S., et al. 2018, *A&A*, **618**, A3
- Rousseau-Nepton, L., Martin, R. P., Robert, C., et al. 2019, *MNRAS*, **489**, 5530
- Rousseau-Nepton, L., Robert, C., Martin, R. P., Drissen, L., & Martin, T. 2018, *MNRAS*, **477**, 4152
- Sana, H., de Mink, S. E., de Koter, A., et al. 2012, *Sci*, **337**, 444
- Scannapieco, C., Wadepuhl, M., Parry, O. H., et al. 2012, *MNRAS*, **423**, 1726
- Schaye, J., Crain, R. A., Bower, R. G., et al. 2015, *MNRAS*, **446**, 521
- Schild, H., Crowther, P. A., Abbott, J. B., & Schmutz, W. 2003, *A&A*, **397**, 859
- Schild, H., & Testor, G. 1992, *A&A*, **266**, 145
- Shimakawa, R., Kodama, T., Steidel, C. C., et al. 2015, *MNRAS*, **451**, 1284
- Smith, N., & Brooks, K. J. 2008, in *The Carina Nebula: A Laboratory for Feedback and Triggered Star Formation*, Vol. 5, ed. B. Reipurth (San Francisco, CA: ASP Monograph Publications), 138
- Stasińska, G., Peña, M., Bresolin, F., & Tsamis, Y. G. 2013, *A&A*, **552**, A12
- Toribio San Cipriano, L., García-Rojas, J., Esteban, C., Bresolin, F., & Peimbert, M. 2016, *MNRAS*, **458**, 1866
- Vogelsberger, M., Genel, S., Springel, V., et al. 2014, *Natur*, **509**, 177
- Vučetić, M. M., Arbutina, B., & Urošević, D. 2015, *MNRAS*, **446**, 943
- Ward, J. L., Chevance, M., Kruijssen, J. M. D., et al. 2019, *MNRAS*, submitted
- Weilbacher, P. M., Monreal-Ibero, A., Kollatschny, W., et al. 2015, *A&A*, **582**, A114
- Weilbacher, P. M., Streicher, O., Urrutia, T., et al. 2012, *Proc. SPIE*, **8451**, 84510B
- Zeidler, P., Nota, A., Sabbi, E., et al. 2019, *AJ*, **158**, 201
- Zeidler, P., Sabbi, E., Nota, A., et al. 2018, *AJ*, **156**, 211